

1 **Revision 1**

2 **Experimental investigation of basalt and peridotite oxybarometers: implications for spinel**
3 **thermodynamic models and Fe³⁺ compatibility during generation of upper mantle melts**

4 Fred A Davis*^{1,2}, Elizabeth Cottrell¹

5 ¹National Museum of Natural History, Smithsonian Institution, Washington, DC 20560, USA

6 ²Department of Earth and Environmental Sciences, University of Minnesota Duluth, Duluth, MN
7 55812, USA

8 *corresponding author, email: fdavis@d.umn.edu; tel: 1-218-726-8331

9 Abstract

10 Peridotites dredged from mid-ocean ridges and glassy mid-ocean ridge basalts (MORB)
11 transmit information about the oxygen fugacity (f_{O_2}) of Earth's convecting upper mantle to the
12 surface. Equilibrium assemblages of olivine+orthopyroxene+spinel in abyssal peridotites and
13 $Fe^{3+}/\Sigma Fe$ ratios in MORB glasses measured by X-ray Absorption Near-Edge Structure (XANES)
14 provide independent estimates of MORB source region f_{O_2} , with the former recording f_{O_2}
15 approximately 0.8 log units lower than the latter relative to the quartz-fayalite-magnetite (QFM)
16 buffer. To test cross-compatibility of these oxybarometers and examine the compositional effects
17 of changing f_{O_2} on a peridotite plus melt system over a range of Earth-relevant f_{O_2} , we performed
18 a series of experiments at 0.1 MPa and f_{O_2} controlled by CO-CO₂ gas mixes between QFM-1.87
19 and QFM+2.23 in a system containing basaltic andesite melt saturated in olivine, orthopyroxene,
20 and spinel.

21 Oxygen fugacities recorded by each method are in agreement with each other and with
22 the f_{O_2} measured in the furnace. Measurements of f_{O_2} from the two oxybarometers agree to
23 within 1 σ in all experiments. These results demonstrate that the two methods are directly
24 comparable and differences between f_{O_2} measured in abyssal peridotites and MORB result from
25 geographic sampling bias, petrological processes that change f_{O_2} in these samples after separation
26 of melts and residues, or abyssal peridotites may not be residues of MORB melting.

27 As f_{O_2} increases, spinel Fe^{3+} concentrations increase only at the expense of Cr from
28 QFM-1.87 to QFM-0.11. Above QFM, Al is also diluted in spinel as the cation proportion of
29 Fe^{3+} increases. None of the three spinel models tested, MELTS (Ghiorso and Sack 1995),
30 SPINMELT (Ariskin and Nikolaev 1996), and MELT_CHROMITE (Poustovetov and Roeder
31 2001), describe these compositional effects, and we demonstrate that MELTS predicts residues

32 that are too oxidized by > 1 log unit to have equilibrated with the coexisting liquid phase. Spinel
33 generated in this study can be used to improve future thermodynamic models needed to predict
34 compositional changes in spinels caused by partial melting of peridotites in the mantle or by
35 metamorphic reactions as peridotites cool in the lithosphere.

36 In our experimental series, where the ratio of $\text{Fe}_2\text{O}_3/\text{FeO}$ in the melt varies while other
37 melt compositional parameters remain nearly constant, experimental melt fraction remains
38 constant and Fe^{3+} becomes increasingly compatible in spinel as f_{O_2} increases. Instead of
39 promoting melting, increasing the bulk $\text{Fe}^{3+}/\Sigma\text{Fe}$ ratio in peridotite drives reactions analogous to
40 the fayalite-ferrosilite-magnetite reaction. This may partly explain the absence of correlation
41 between Na_2O and Fe_2O_3 in fractionation-corrected MORB.

42 **Introduction**

43 Basalts and peridotites convey information about the chemical activity of oxygen in
44 Earth's mantle, commonly expressed through the thermodynamic variable oxygen fugacity (f_{O_2}).
45 Oxygen fugacity is important for understanding solubility and speciation of redox-sensitive
46 volatile elements in mid-ocean ridge basalt (MORB) magmas and for anchoring extrapolation of
47 the f_{O_2} -depth profile through Earth's upper mantle (Stagno and Frost 2010; Stagno et al. 2013)
48 with consequences for the depth of melting (Dasgupta et al. 2013) and the depth of metal
49 saturation (O'Neill and Wall 1987; Ballhaus 1995; Rohrbach et al. 2011).

50 Mineral equilibria in abyssal peridotites dredged from the mid-ocean ridge system and
51 $\text{Fe}^{3+}/\Sigma\text{Fe}$ ratios of MORB glasses record information about f_{O_2} conditions in the sub-ridge
52 mantle. These two sources of f_{O_2} information are independent; they rely on different samples,
53 different thermodynamic f_{O_2} models, and different analytical techniques. Because some

54 geochemical and geophysical inferences about the Earth depend on the absolute value of mantle
55 f_{O_2} , for example, the depth to the diamond/graphite to carbonated melt reaction (Stagno et al.
56 2013), it is useful to consider the extent to which these two independent mantle f_{O_2} proxies agree.
57 In this contribution, we compare results from the seminal study of Bryndzia and Wood (1990) on
58 the f_{O_2} of abyssal peridotites, to results from (Zhang et al. 2018), which updates the study of
59 Cottrell and Kelley (2011) on the f_{O_2} of MORB. The two global data sets do not appear to be in
60 agreement about prevailing f_{O_2} conditions in the MORB source. Abyssal peridotites record a
61 mean $\log f_{O_2}$ 0.9 log units below the quartz-fayalite-magnetite buffer (QFM-0.9±0.7) and a range
62 from QFM-2.5 to QFM+0.5 (Bryndzia and Wood 1990), while MORB glasses record a mean of
63 QFM-0.18±0.16 and range from QFM-0.7 to QFM+0.3 (Cottrell and Kelley 2011; Zhang et al.
64 2018). The apparent incongruence between melt-based and residue-based oxybarometers in
65 nature indicates that our understanding of peridotite + melt assemblages as a function of f_{O_2} is
66 nascent. The limited geographic distribution of peridotites, or the fact that peridotites and basalts
67 from the same ridge segment have not been analyzed, may lead to sampling bias. It may be too
68 that the assumption that these rocks are genetically related could be incorrect (e.g., Rampone et
69 al. 1998). Or, the incongruence may result from a systematic offset between the two independent
70 oxybarometers used to assess f_{O_2} : Bryndia and Wood (1990) applied spinel oxybarometry to
71 abyssal peridotites; Zhang et al. (2018) calculated f_{O_2} from silicate melt Fe^{3+}/Fe^{2+} ratios
72 determined by Fe K-edge X-ray Absorption Near-Edge Structure (XANES) spectroscopy
73 (Cottrell and Kelley, 2011) via the algorithm of Kress and Carmichael (1991). We address this
74 final possibility in this contribution.

75 In this paper, we report laboratory experiments that equilibrate basaltic-andesite melts
76 with a solid assemblage of olivine+orthopyroxene+spinel over a range of f_{O_2} . We analyzed

77 resulting spinel $\text{Fe}^{3+}/\Sigma\text{Fe}$ ratios by electron probe microanalysis (EPMA) using Mössbauer-
78 characterized spinel standards for data-correction (Wood and Virgo 1989; Davis et al. 2017) and
79 glass $\text{Fe}^{3+}/\Sigma\text{Fe}$ ratios by XANES (Cottrell et al. 2009; Zhang et al. 2018). These experiments
80 allow to examine the chemistry of peridotite plus melt in a system with known, externally-
81 imposed f_{O_2} . Importantly, we are able to explore how the compositions of spinels in equilibrium
82 with peridotite change with f_{O_2} . We compare these changes with three popular thermodynamic
83 models for spinel and reveal broad consequences for melt generation in the upper mantle.

84 **Methods**

85 *Experimental methods*

86 We made two starting materials intended to generate an equilibrium assemblage of
87 olivine, orthopyroxene, spinel, and basaltic melt. The first starting material, “LOOS”, produced
88 run products with tiny spinel grains that made it difficult to find crystal-free glass pools for micro
89 analysis. As a result, we present only a single experiment with this first starting material. We
90 modeled starting mix “LOOS” on the run products of experiment 85-41c#4 from (Grove et al.
91 2003), which is one of only twenty experiments in the Library of Experimental Phase Relations
92 (Hirschmann et al. 2008) saturated in all of these phases at 0.1 MPa.

93 We made two minor adjustments to the phase compositions before determining the bulk
94 composition of the starting material. The glass in 85-41c#4 has 56.8 wt.% SiO_2 , which is higher
95 than the SiO_2 concentration range (48.06-52.91 wt.%) of the experimental and natural basalts
96 used by Cottrell et al. (2009), Cottrell and Kelley (2011), and Zhang et al. (2018) to demonstrate
97 comparability of $\text{Fe}^{3+}/\Sigma\text{Fe}$ ratios in glasses determined by XANES to $\text{Fe}^{3+}/\Sigma\text{Fe}$ ratios determined
98 by wet chemical analysis and Mössbauer spectrometry. We attempted to bring the composition

99 of our experimental glasses closer to the SiO₂ range of MORB by increasing the concentration of
100 TiO₂ in the melt component to 3 wt.%, just outside the range of TiO₂ concentrations in the
101 Cottrell and Kelley group's glasses (0.62-2.56 wt.%). Addition of this amount of TiO₂ is
102 expected to diminish SiO₂ of a liquid saturated in olivine and orthopyroxene by about 1 wt.%
103 (Xirouchakis et al. 2001). Because spinel also dissolves appreciable TiO₂, so we also added TiO₂
104 to the spinel component in an amount suggested by the experiment spinel/melt partition
105 coefficient defined by the phases in 85-41c#4. After making these modifications to the phase
106 components we calculated a bulk composition with the following proportions by weight: 70%
107 melt, 10% olivine, 10% opx, 10% spl.

108 We generated starting material LOOS2, which includes less of the spinel component, in
109 an attempt to counteract abundant nucleation of spinel crystals. The bulk composition for
110 LOOS2 was calculated with the following proportions by weight: 72% melt, 10% olivine, 15%
111 opx, 3% spl.

112 We mixed each of the starting materials from reagent oxide powders of SiO₂, TiO₂,
113 Al₂O₃, Cr₂O₃, MgO, MnCO₃, Fe₂O₃, CaCO₃, Na₂CO₃, K₂CO₃, and V₂O₃. We fired most of these
114 powders before mixing to remove surface adsorbed water for the following times and
115 temperatures: SiO₂ at 1250 °C for 8 hours, Al₂O₃ and MgO at 1200 °C for 88 hours, TiO₂ at
116 1000 °C for 16 hours, CaCO₃, Na₂CO₃, and K₂CO₃ at 400 °C for 4, 12, and 8 hours respectively.
117 We weighed all oxides except Cr₂O₃ and Fe₂O₃ and ground them in an agate mortar under
118 ethanol for about one hour. This mixture was then decarbonated in air by ramping temperature at
119 100 °C per hour to 1000 °C and dwelling for 12 hours. Weight of powders after the
120 decarbonation step indicated that all CO₂ was driven off the powder. We then added to the
121 mixture Cr₂O₃ and Fe₂O₃ and ground the combined mixture in an agate mortar under ethanol for

122 about one hour. The final powder was stored in a desiccator. The compositions of the starting
123 mixtures are given in Table 1.

124 We performed the experiments in DelTech vertical-tube gas mixing furnaces at the
125 Smithsonian Institution National Museum of Natural History. We controlled oxygen fugacity
126 using a mixture of CO and CO₂ gases and monitored f_{O_2} during the experiment using a ZrO₂-Pt
127 oxygen sensor, referenced to O₂ gas. We calibrated the sensor against a gas mixture of 50% CO,
128 50% CO₂. Log f_{O_2} was controlled to within ± 0.05 log units, with the exception of experiment
129 LOOS2_2A, which experienced anomalous fluctuations in EMF we describe below.
130 Temperature inside the furnace tube was monitored using a PtRh thermocouple and controlled to
131 within ± 2 °C of 1225 °C. The hottest region of the furnace was mapped by moving the
132 thermocouple through the hotspot. The thermocouple was calibrated against the melting point of
133 Au wire. Experimental charges were hung from Pt-loops by mixing starting powders with
134 polyvinyl alcohol and partially fusing in air at 1400 °C. Each Pt loop was pre-saturated in Fe by
135 equilibrating with experimental starting powder at the run temperature and gas mix of each
136 experiment for 16-48 hours. After pre-saturation, run products were removed from the loops by
137 soaking in hydrofluoric acid overnight. Pt loops were then reloaded with starting powder and
138 hung in the furnace under the conditions given in Table 2. Experiments were rapidly quenched
139 by dropping the loop into a water bath without exposing the samples or gas mix in the furnace to
140 air. We mounted experiments in epoxy and cut in half. One side was polished for electron
141 microprobe analysis. The other half was double-side polished for analysis by XANES.

142 Experiment LOOS2_2A was held at an f_{O_2} of QFM+2.23 \pm 0.05 for the first 69 hours of
143 the run, but upon checking the EMF before quench, furnace f_{O_2} was found to be fluctuating
144 anomalously at QFM+2.36 \pm 0.15. These fluctuations may have been occurring for as long as the

145 last two hours of the run. We have accounted for this fluctuation by presenting a larger
146 uncertainty in furnace f_{O_2} for this experiment.

147 *Electron microprobe analysis*

148 Electron imaging (Figure 1) was performed using a JEOL JXA-8530F Hyperprobe field-
149 emission gun electron microprobe at the Smithsonian Institution. Glasses and minerals were
150 analyzed for major elements by electron microprobe at the Smithsonian Institution using a JEOL
151 8900 Superprobe with 5 wavelength dispersive spectrometers (WDS). We analyzed the K_α peaks
152 of the following elements: SiO_2 , TiO_2 , Al_2O_3 , Cr_2O_3 , FeO^* (ΣFe calculated as FeO), MnO , MgO ,
153 CaO , Na_2O , and K_2O . Glasses, olivines, and orthopyroxenes were analyzed using an accelerating
154 voltage of 15 kV. Spinel were analyzed using an accelerating voltage of 13 kV in an attempt to
155 excite a smaller volume, except spinels from LOOS_0B, which were analyzed with a 15 kV
156 accelerating voltage. We analyzed glasses with a 10 μm diameter defocused spot and a 10 nA
157 beam current. We analyzed minerals with a focused beam ($\sim 1 \mu m$ dia.) and beam current of 40
158 nA, except olivines from LOOS_0B, which were analyzed with a 15 nA beam current. We used
159 the Armstrong/Love-Scott ZAF procedure for matrix correction (Armstrong 1988). Because
160 orthopyroxene and spinel grains were small ($< 5 \mu m$ diameter), only one analytical point was
161 collected for any given grain. Olivines were much larger, which allowed analysis of 3-5 points
162 per grain on 3-5 total grains. Supplementary Table S1 provides information on our primary
163 standards, count times, and detector crystals. We selected peak positions for each element at the
164 beginning of each analytical session by performing a wavelength scan in the region of the peak.
165 We counted both peaks and backgrounds at each analytical point (Supplemental Table S1).

166 Spinel crystals were so small (largest $< 3 \mu m$ across) that, even when analyzing at 13 kV,
167 surrounding silicate glass was commonly sampled in the excitation volume. We analyzed only

168 spinel crystals surrounded by glass and none that were partially or wholly included in olivine
169 crystals. Resulting analyses were mixtures of varying proportions of spinel and glass
170 compositions. We were able to remove analyses significantly sampling glass by discarding
171 individual analyses that had Na₂O concentrations ≥ 0.05 wt.%. Davis et al. (2017) found that
172 Na₂O was not present above the limit of detection (~ 0.01 wt.% under these analytical conditions)
173 in any of the spinels analyzed in that study, so we expect that the actual Na₂O concentrations in
174 spinels are negligible. After removing these obviously glass influenced analyses we still found
175 that SiO₂ and CaO concentrations in the spinel were much higher (SiO₂ > 0.5 wt.%; CaO > 0.2
176 wt.%) than have been observed in many studies of natural spinels that report concentrations for
177 these oxides (SiO₂ < 0.2 wt.%, Canil et al. 1990; Ionov and Wood 1992; Woodland et al. 1992;
178 Luhr and Aranda-Gómez 1997; Brunelli et al. 2006; Warren and Shimizu 2010; CaO < 0.05
179 wt.%, Canil et al. 1990; Parkinson and Pearce 1998; Davis et al. 2017); although, there are a few
180 examples where higher SiO₂ has been reported (SiO₂ between 0.7 and 1.5 wt.%, Johnson and
181 Dick 1992; Parkinson and Pearce 1998). Spinel from experiment 85-41c#4 of Grove et al.
182 (2003), upon which our experimental starting material was based and generated under similar
183 experimental conditions, was reported to have SiO₂ = 0.18 \pm 0.37 wt.% and CaO = 0.10 \pm 0.005
184 wt.%, further suggesting our observed high SiO₂ and CaO concentrations are anomalous. We
185 attribute this excess SiO₂ and CaO in the analysis to secondary fluorescence of the surrounding
186 glass. Secondary fluorescence of elements in low abundance is commonly observed in analyses
187 of minerals included in a matrix with elevated abundances of those elements (e.g., (Bastin et al.
188 1983; Llovet et al. 2000)), and is likely an unavoidable consequence of analyzing experimental
189 spinels < 3 μ m in size using electron beam methods. Because excess SiO₂ and CaO in the spinel
190 analysis can have a large effect on calculated Fe³⁺/ Σ Fe ratios, especially if secondary

191 fluorescence contributions from the two are not equal in magnitude, and because SiO₂ and CaO
192 concentrations in these spinels are expected to be low, we have chosen to omit SiO₂ and CaO
193 from our stoichiometric calculations of spinel Fe³⁺/ΣFe ratios (described below). Full EPMA
194 analyses of spinels including SiO₂, CaO, and Na₂O are given in Supplementary Table S2.

195 Fe³⁺/ΣFe ratios in spinels were determined from the electron microprobe analyses
196 following the method of (Davis et al. 2017), which is a modification of the method presented by
197 (Wood and Virgo 1989). Fe³⁺/ΣFe ratios of each spinel were calculated from spinel
198 stoichiometry by normalizing the spinel cation proportions to 3 total cations, initially treating all
199 Fe as Fe²⁺, and then adjusting the Fe³⁺/Fe²⁺ ratio to balance the charge deficiency or excess
200 (Stormer 1983). These initial estimates of Fe³⁺/ΣFe ratios were then corrected by comparison to a
201 set of spinel standards with Fe³⁺/ΣFe ratios previously determined by Mössbauer spectrometry
202 (Wood and Virgo 1989; Bryndzia and Wood 1990; Ionov and Wood 1992). The correction
203 standards were analyzed at the beginning and end of each analytical session and a linear
204 correction was defined by the relationship between Cr# (Cr/[Cr+Al]) and the difference between
205 Fe³⁺/ΣFe ratio determined by Mössbauer and by electron microprobe ($\Delta\text{Fe}^{3+}/\Sigma\text{Fe}^{\text{Möss-EPMA}}$). The
206 correction was applied to all analyses of the experimental spinels irrespective of whether Cr# and
207 $\Delta\text{Fe}^{3+}/\Sigma\text{Fe}^{\text{Möss-EPMA}}$ of the correction standards were found to be correlated (see discussion in
208 Davis et al. 2017). Complete analyses of correction standards are given in Supplemental Table
209 S3.

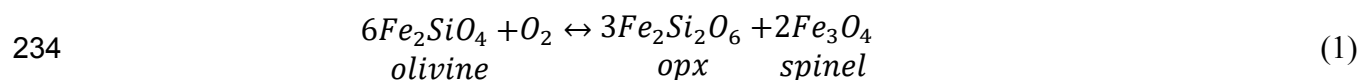
210 *X-ray absorption near-edge structure (XANES) analysis of Fe³⁺/ΣFe ratios in glasses*

211 We measured Fe³⁺/ΣFe ratios in experimental glasses using XANES at bending magnet
212 beamline X26A at the National Synchrotron Light Source, Brookhaven National Laboratory,
213 USA, following the method and basalt glass standards of (Cottrell et al. 2009). Before XANES

214 analysis, the section of each experiment intended for XANES was double-polished to optical
215 transparency (<100 μm), and epoxy was removed by bathing in acetone. Reference glass LW_0
216 was analyzed to correct for energy drift related to the thermal load on the Si (311)
217 monochromator (Cottrell et al. 2009). We evaluated the spectra for crystal interference
218 (Supplemental Figure S1), and discarded spectra with evidence for crystal interference. The
219 photon flux density at X26A was 6×10^7 photons/sec/ μm^2 . Synchrotron radiation, at photon flux
220 densities at least as high as 1×10^{13} photons/sec/ μm^2 , does not cause beam damage (oxidation or
221 reduction) to Fe in anhydrous glasses (Cottrell et al. 2018). $\text{Fe}^{3+}/\Sigma\text{Fe}$ ratios in the glass were
222 calculated from the drift-corrected centroids (area-weighted average energy of the pre-edge
223 doublet in the XANES spectra) collected from the glasses according to the method of Cottrell et
224 al. (2009), using the basalt calibration curve of Zhang et al. (2018). The Zhang et al. (2018)
225 calibration accounts for the recoilless fraction in the Mossbauer spectra used to determine the
226 $\text{Fe}^{3+}/\Sigma\text{Fe}$ ratios of the glass standards, making the Fe XANES measurements more accurate
227 without sacrificing precision. We analyzed three independent points on each glass and measured
228 centroids with a precision of $1\sigma = 0.013 \pm 0.006$ eV and $\text{Fe}^{3+}/\Sigma\text{Fe}$ ratios of $1\sigma = 0.005 \pm 0.003$
229 (Table 4). XANES spectra are shown in Supplementary Figure S2.

230 *Calculation of oxygen fugacity*

231 We calculated f_{O_2} recorded by the experimental run products from the chemical
232 compositions of olivine, orthopyroxene, and spinel and, independently, from the $\text{Fe}^{3+}/\Sigma\text{Fe}$ ratio
233 of the glass. For the mineral assemblage, f_{O_2} can be calculated from the following equilibrium:



235 We calculated f_{O_2} in bars using the following equation from Davis et al. (2017), which was
236 derived from equations presented in Mattioli and Wood (1988) and Wood and Virgo (1989):

$$\log(f_{O_2})_{P,T} = \frac{-24222}{T} + 8.64 + \frac{0.0567P}{T} - 12 \log(1 - Mg\#^{ol}) - \frac{2620}{T} (Mg\#^{ol})^2$$

237 $+ 3\log(X_{Fe}^{M1} \cdot X_{Fe}^{M2})^{opx} + 2\log(a_{Fe_3O_4}^{spl})$ (2)

238 We used the same procedures to calculate each compositional variable in this equation as in
239 Davis et al. (2017). We calculated f_{O_2} recorded by the $Fe^{3+}/\Sigma Fe$ ratio of the glass using equation
240 6 from (Kress and Carmichael 1991). When we compare $\log f_{O_2}$ to the QFM buffer we use the
241 formulation of (Frost 1991).

242 *Spinel compositional modeling*

243 Several models can predict spinel compositions given an equilibrium melt composition.
244 We have generated model spinel compositions for comparison with our experimental results
245 using MELTS (Ghiorso and Sack 1995), SPINMELT (Ariskin and Nikolaev 1996), and MELT-
246 CHROMITE (Poustovetov and Roeder 2001). We modeled spinel compositions in MELTS
247 through the alphaMELTS application (Asimow and Ghiorso 1998; Smith and Asimow 2005).
248 For each experiment we input the composition of the glass measured by electron microprobe
249 with all Fe as FeO, initialized the system at 0.1 MPa and 1225 °C, and held f_{O_2} constant at the
250 value measured in the furnace. We initialized the phase equilibria at 1225 °C and then ran an
251 isobaric, closed system (batch crystallization) cooling path to 1200 °C at temperature increments
252 of 1 °C.

253 SPINMELT is not available as a stand-alone program and the corresponding author could
254 not be reached. Our attempts to code SPINMELT from the information supplied in (Ariskin and

255 Nikolaev 1996) did not reproduce the results given in that paper, so we ran SPINMELT through
256 PETROLOG 3.1.1.3 (Danyushevsky and Plechov 2011). In Petrolog 3, we performed
257 crystallization runs with spinel as the only crystallizing phase and (Ariskin and Nikolaev 1996)
258 selected as the spinel compositional model. We set P to 0.1 MPa and f_{O_2} to the value measured in
259 the furnace. We selected (Kress and Carmichael 1988) as the melt Fe^{3+}/Fe^{2+} model and set
260 fractionation of spinel to 0%. For each experiment we input the composition of the glass
261 measured by electron microprobe with all Fe as FeO.

262 MELT-CHROMITE predicts a spinel composition in terms of five compositional
263 components if given a melt composition, temperature, and pressure; it does this by
264 simultaneously solving four empirically-derived equations for compositional variables in the
265 melt (Poustovetov and Roeder 2001). We solved these four equations in Microsoft Excel using
266 the Solver add-in (Evolutionary mode) to minimize the sum of square residuals between the melt
267 compositions and the equation outputs. We input glass compositions measured by electron
268 microprobe with all FeO and Fe_2O_3 as determined by XANES, temperature of 1225 °C, and
269 pressure of 0.1 MPa.

270 **Results**

271 *Melt and mineral phase textures, compositions, and modal proportions*

272 Each experiment produced an assemblage of olivine, orthopyroxene, Cr-rich spinel, and
273 basaltic glass (Figure 1). Olivines formed euhedral crystals typically 40-60 μm across in the
274 shortest direction. Orthopyroxenes formed small elongate grains <10 μm in width and <30 μm in
275 length. Olivines and orthopyroxenes have quench rims (<300 nm) but show no evidence of large-
276 scale chemical zonation. Spinel formed small grains <3 μm across.

277 Spinel compositions vary considerably with increasing f_{O_2} . It is most convenient to
278 examine spinel compositions in terms of major cations separated by stoichiometric units because
279 it allows for us to see which trivalent cations are substituting for Fe^{3+} as experimental f_{O_2} varies.
280 Spinel has the general formula AB_2O_4 , where generally, A-type cations are divalent and B-type
281 cations are trivalent; although, the ulvöspinel endmember ($TiFe_2O_4$) has Ti^{4+} as the A cation and
282 Fe^{2+} as the B cation. After calculating spinel compositions per three total cations as described in
283 Methods, a portion of the Fe^{2+} cations equal to two times the concentration of Ti cations was
284 allocated to the B cations, and the remaining Fe^{2+} is allocated to the A cations. All Ti and Mg
285 were assigned to A, and all Al, Cr, and Fe^{3+} were assigned to B.

286 Spinel compositions are presented in Figure 2 in units of cations per three total cations.
287 Spinel A-type cations show little variation between QFM-1.87 and QFM+1.40 (Figure 2a).
288 Above QFM+1.40, Mg concentration increases, while Fe^{2+} decreases, consistent with the
289 increase in Mg# observed in the coexisting liquid and olivine in that experiment (described
290 below). Ti also decreases above QFM+1.40. Fe^{3+} increases as a proportion of the B-type cations
291 as $\log f_{O_2}$ increases (Figure 2b). This increase is approximately linear below QFM+1, but at
292 higher f_{O_2} , more Fe^{3+} enters spinel per log unit increase in f_{O_2} . Cr concentration decreases
293 linearly with increasing $\log f_{O_2}$ ($R^2=0.63$, p-value = 0.019), Al remains roughly constant from
294 QFM-1.87 to QFM-0.11, but begins to decrease in concentration above at $f_{O_2} > QFM$, and Fe^{2+} ,
295 which is tied to Ti in our calculation, remains constant from QFM-1.87 to QFM+1.40,
296 decreasing only in the most oxidized experiment.

297 Several oxides in the glasses vary systematically with f_{O_2} (Figure 3). SiO_2 ($R^2 = 0.77$, p-
298 value = 0.004), TiO_2 ($R^2 = 0.76$, p-value = 0.005), Al_2O_3 ($R^2 = 0.71$, p-value = 0.009) all
299 decrease in the melt with increasing f_{O_2} , while Fe_2O_3 ($R^2 = 0.79$, p-value = 0.003) increases.

300 Cr₂O₃ concentrations in the glass from experiment LOOS_0B, the only experiment run using the
301 very Cr-rich LOOS starting mix (Table 1), is greater than Cr₂O₃ concentrations in melts from
302 LOOS2 experiments. When only experiments run on LOOS2 are considered, Cr₂O₃ decreases
303 systematically in the melt with increasing f_{O_2} ($R^2 = 0.62$, p-value = 0.04). Other elements,
304 notably the incompatible elements CaO, Na₂O, and K₂O, show no systematic variation with f_{O_2} .

305 Because all of the experiments are saturated in olivine and orthopyroxene of similar
306 compositions, the activity of SiO₂ is nearly fixed. Therefore, decreasing SiO₂ with f_{O_2} in the
307 glasses suggests a role for Fe³⁺ as a network former in these glasses. The relationship between
308 SiO₂ in the melt and f_{O_2} observed in these experiments suggests a significant fraction of Fe³⁺ may
309 be tetrahedrally coordinated, consistent with studies of iron coordination in glass (e.g., Wilke et
310 al. 2005). We observe a corresponding effect in the modal proportions of olivine and
311 orthopyroxene, described below. On the other hand, we note that SiO₂ and Fe₂O₃ in the glass are
312 not themselves significantly correlated ($R^2 = 0.42$, p-value = 0.08), therefore the causes of the
313 correlation between SiO₂ and $\log f_{O_2}$ may be more complex than simple addition of Fe³⁺ to the
314 melt.

315 With the exceptions of Mg# and Cr₂O₃ concentration, olivine and orthopyroxene
316 compositions vary little with f_{O_2} . Given that the Fe³⁺/ΣFe ratio of the liquid increases
317 dramatically while total FeO increases only moderately, we expect that the Mg/Fe²⁺ ratio of the
318 melt, and therefore Mg# in the olivine, should increase with f_{O_2} . However, we do not observe a
319 significant correlation between olivine Mg# and $\log f_{O_2}$ ($R^2 = 0.41$, p-value = 0.09, Figure 4). It
320 is likely that increasing f_{O_2} does lead to an increase in olivine Mg#, but the effect is obscured by
321 Fe-loss from the system, which has affected the most reduced experiment to a greater degree
322 (almost a factor of 2 greater) than the more oxidized experiments (Table 2). When we exclude

323 the most reduced experiment (LOOS2_-2A) we find that Mg# in the remaining olivines does
324 correlate with $\log f_{O_2}$ ($R^2 = 0.86$, p-value = 0.003). Mg# in this subset of the experiments
325 increases about 0.005 per log unit increase in f_{O_2} (Figure 4b), corresponding to an increase in
326 Mg# of about 0.02 over the four orders of magnitude change in f_{O_2} that we explored in this study.
327 A similar correlation between Mg# in orthopyroxene and $\log f_{O_2}$ is not observed.

328 Cr_2O_3 concentrations, as in the glass, generally decrease in olivine and orthopyroxene
329 with increasing f_{O_2} . Again, Cr_2O_3 in both phases is highest in LOOS_0B, which used the higher
330 Cr starting material. When we consider Cr_2O_3 from the perspective of mineral/melt partitioning,
331 we find that olivine/melt and orthopyroxene/melt Cr partition coefficients are approximately
332 constant ($D_{Cr}^{ol}=1.3\pm 0.2$ and $D_{Cr}^{opx}=7.5\pm 1.5$). This constant partitioning relationship suggests that
333 most of the Cr is trivalent in our experiments, roughly consistent with the observations of
334 Mallmann and O'Neill (2009) who observed a decrease in D_{Cr}^{opx} at $f_{O_2} < QFM-1$. Our
335 experiments do not extend to low enough f_{O_2} to make any further observations about Cr.

336 We calculated modal proportions of each phase by weight using multiple linear
337 regression (Table 2, Figure 5). The regression included a pure Fe phase to allow for an estimate
338 of Fe-loss to the Pt loop. Phase proportions determined in this way always summed to between
339 99.7 and 99.9%. Modal proportions of phases were renormalized to exclude Fe lost to the Pt
340 loop. Because one experiment uses the LOOS starting material, its modal phase proportions
341 cannot be directly compared to those of the other experiments; therefore, we refer only to the
342 phase proportions of the experiments from the LOOS2 series here. The percent of melt in the
343 experiments is nearly constant over the range of f_{O_2} examined (Figure 5a) with an average of
344 $75.2\pm 0.6\%$. Modal spinel increases with increasing $\log f_{O_2}$ (Figure 5b). Although the absolute
345 increase is small (2.8-3.2%) the correlation is significant ($R^2 = 0.96$, p-value = 8×10^{-5}) and the

346 change represents a 14% relative increase in modal spinel. Modal olivine decreases ($R^2 = 0.78$,
347 p-value = 0.009) and modal orthopyroxene increases ($R^2 = 0.61$, p-value = 0.04) as $\log f_{O_2}$
348 increases, consistent with decreasing SiO_2 in the liquid as f_{O_2} increases.

349 *Oxygen fugacities recorded by glasses and minerals*

350 Calculations of f_{O_2} from the solid assemblage and from the $Fe^{3+}/\Sigma Fe$ ratios of the glasses
351 are in agreement with the f_{O_2} of the gas mix monitored during the experiments and are in
352 agreement with each other. We compare $\log f_{O_2}$ relative to QFM calculated from the solid
353 assemblage to $\log f_{O_2}$ of the gas mix in Figure 6a. These independent assessments of system f_{O_2}
354 are highly correlated ($R^2 = 0.96$, p-value = 2×10^{-5}) with a slope near unity ($m = 0.85 \pm 0.07$) and a
355 y-intercept near zero ($b = -0.19 \pm 0.09$). The average difference between $\log f_{O_2}$ of the furnace and
356 $\log f_{O_2}$ calculated by spl-oxybarometry is -0.22 ± 0.31 log units, similar to the offset from furnace
357 f_{O_2} observed in the experiments of Wood (1990). We compare $\log f_{O_2}$ calculated from the
358 $Fe^{3+}/\Sigma Fe$ ratios of the glasses to $\log f_{O_2}$ of the gas mix in Figure 6b. These assessments of system
359 f_{O_2} are similarly highly correlated ($R^2 = 0.91$, p-value = 2×10^{-4}) and nearly coincide with a 1:1
360 line ($m = 1.03 \pm 0.13$ and $b = -0.23 \pm 0.17$). The average difference between $\log f_{O_2}$ of the furnace
361 and $\log f_{O_2}$ calculated from the glass $Fe^{3+}/\Sigma Fe$ ratios is -0.23 ± 0.43 log units. Glass from
362 experiment LOOS2_2A records a notably higher f_{O_2} than the furnace environment, even as the
363 mineral assemblage accurately records furnace f_{O_2} . It is possible that this offset is related to
364 fluctuations in furnace f_{O_2} in the final 2 hours of that experiment (described in Methods) which
365 may have led to oxidation of the melt phase, but did not have time to be diffusively transmitted
366 to the solids. We have also compared the two oxybarometers to each other (Figure 6c),
367 demonstrating their close agreement. Results of the two oxybarometers are correlated ($R^2 = 0.90$,

368 p -value = 3×10^{-4}) and adhere closely to the 1:1 line ($m = 1.17 \pm 0.16$ and $b = 0.00 \pm 0.18$).

369 Measurements of f_{O_2} from the two oxybarometers agree to within 1σ in all experiments.

370 *Results of spinel compositional models*

371 MELTS outputs predicted spinel to be a coexisting phase at 1225 °C in all but two of the
372 model runs, and in each of the others spinel saturation was achieved by 1209 °C. MELTS also
373 predicted orthopyroxene crystallization over this temperature interval in all runs and olivine
374 saturation in two runs (Supplemental Table S4). For each SPINMELT calculation run in Petrolog
375 3, a temperature of spinel saturation and a spinel composition were output (Supplemental Table
376 S5). Four of the eight compositions gave saturation temperatures within ± 10 °C of 1225 °C. The
377 other compositions gave spinel saturation temperatures 1269 °C $< T < 1291$ °C, so differences in
378 temperature between the experiments and the Petrolog output are expected to be minor.
379 Compositions output by MELT-CHROMITE are in Supplementary Table S6. Model spinel
380 compositions are compared to experimental spinels in Figure 7. We discuss these model
381 compositions below.

382 **Discussion**

383 *Using spinel peridotite oxybarometry and glass $Fe^{3+}/\Sigma Fe$ ratios from XANES to investigate f_{O_2} in*
384 *Earth's upper mantle*

385 Our experimental results suggest that when basaltic glasses and spinel peridotites are
386 known to be in equilibrium, Fe-XANES of the glass and spinel oxybarometry give congruent
387 results. Although the ranges of MORB-derived and peridotite-derived f_{O_2} overlap in nature, the
388 mean f_{O_2} of the peridotite dataset is significantly lower than the Zhang et al. (2018) basalt dataset
389 (t-test p -value $\ll 0.0001$; Figure 8) or the wet-chemistry-derived Bézous and Humler (2005)

390 dataset (t-test p-value = 0.001). Our experimental results suggest that the incongruence between
391 the $\log f_{O_2}$ records of MORB glasses and abyssal peridotites is not due to systematic differences
392 between the two methods of determining $\log f_{O_2}$. Instead, these samples record real differences in
393 $\log f_{O_2}$ at the time that the f_{O_2} records were frozen in.

394 *Dependence of spinel compositions on f_{O_2}*

395 Olivine, orthopyroxene, and melt compositions in these experiments vary little over 4 log
396 units of f_{O_2} ; thus, the chemical variation we observe in the spinels reflects changes only in liquid
397 $Fe^{3+}/\Sigma Fe$ ratios resulting from increasing f_{O_2} . Even the small systematic chemical variations
398 observed in the other phases occur in a system with equilibrium olivine and orthopyroxene, and,
399 therefore, reflect chemical changes to a peridotite-saturated system that are inextricable from
400 changes in f_{O_2} . For example, the ~2 wt.% decrease in SiO_2 in the melt from the most reducing to
401 the most oxidizing experiments reflects changes in the melt composition due to increased Fe^{3+} in
402 the melt while activity of SiO_2 is held constant by equilibrium between olivine and
403 orthopyroxene. These experimental spinels, then, can provide direct insights into how spinel
404 compositions in spinel peridotites evolve as f_{O_2} of the system is perturbed at 0.1 MPa and
405 constant temperature.

406 Our experimental study is unique in the sense that it examines compositional effects of
407 f_{O_2} on a peridotite plus melt system over a range of f_{O_2} conditions comparable to those found in
408 magmatic systems on Earth. As mentioned in Methods, there are only 20 experiments in the
409 LEPR database with an assemblage of melt+olivine+orthopyroxene+spinel at 0.1 MPa and
410 controlled f_{O_2} . Of those 20, 15 are from a single study by Barnes (1986) with f_{O_2} varying from
411 QFM-3.81 to QFM+0.75 and temperatures from 1157 °C to 1323 °C. A comparison of our spinel
412 compositions with the spinels from Barnes (1986) within ± 50 °C of our experimental

413 temperature of 1225 °C shows close agreement over the range at which the experiments overlap.
414 But the most interesting compositional changes we have observed occur at $f_{O_2} > \text{QFM}+1$ where
415 Fe^{3+} begins to dilute the concentration of Al and Ti in the spinel in addition to Cr (Figure 4), and
416 there are no peridotite-saturated data for direct comparison under these conditions.

417 Ballhaus et al. (1991) performed peridotite-saturated experiments over a range of f_{O_2} at
418 pressures between 0.3 and 2.7 GPa using several different bulk compositions, but whether these
419 experiments show similar compositional trends to what we have observed in this study is
420 ambiguous. Spinel produced by the different starting materials at any given pressure in the
421 Ballhaus et al. (1991) study variably show no change in Al in spinel with f_{O_2} (mix S1297 at 2.5
422 GPa), steadily decreasing Al with f_{O_2} (mix MPY30 at 1 GPa), or steady Al at low f_{O_2} and steep
423 decreases in Al at higher f_{O_2} (mix MPY30 at 2.5 GPa). Comparison of these results with our
424 experiments is complicated because temperature varies over a range >200 °C in most
425 combinations of starting material and pressure, and only one of these combinations has a total
426 number of experiments greater than 4. There are 6 experiments from Ballhaus et al. (1991) run
427 using mix MPY30 at 2.5 GPa and within ± 50 °C of 1100 °C. These experiments produced spinel
428 with an approximately constant Al concentration below QFM+3 as Fe^{3+} increased steadily, and
429 then a steep decrease in Al at higher f_{O_2} , similar to what we observe in our 0.1 MPa experiments
430 above QFM+1. There is clearly need for more experiments in peridotite saturated systems at a
431 range of f_{O_2} and pressures to better define f_{O_2} dependence of spinel compositions.

432 We compare model spinel compositions from MELTS (Ghiorso and Sack 1995; Smith
433 and Asimow 2005), SPINMELT (Ariskin and Nikolaev 1996), and MELT-CHROMITE
434 (Poustovetov and Roeder 2001) to the compositions of experimental spinels from this study in
435 Figure 7. We also modeled spinel compositions in pMELTS (Ghiorso et al. 2002), but resulting

436 spinels were less accurate than MELTS output, and we do not discuss them further. There are
437 two important aspects of the model outputs that we want to consider: 1. How accurately do the
438 models reproduce the compositions of the experimental spinels, and 2. How well do the models
439 predict changes in the exchange reactions between spinel and melt? The second question in
440 particular is important for assessing how likely it is that a model will be able to predict
441 conditions outside its calibration data set or how well the model will be able to predict behavior
442 in a dynamic system.

443 The model spinels produced by MELTS are the least accurate of the three models
444 considered; however, MELTS captures changes in the exchange reactions observed in the
445 experiments that the other models do not. MELTS over-predicts the concentrations of Fe³⁺
446 (+0.05 to +0.49 cations per formula unit) and of the ulvöspinel component (+0.08 to +0.15 Fe²⁺
447 cations per formula unit), while under-predicting Cr concentration (-0.09 to -0.63 cations per
448 formula unit). But MELTS captures the change in Al with f_{O_2} the best of the three models
449 considered, both in accuracy for any given melt- f_{O_2} pair and in the overall topology of the curve
450 (Figure 7a). All model spinels produced by MELTS have Al concentrations within ± 0.09 cations
451 per formula unit of the corresponding experimental spinel. Most importantly, MELTS predicts
452 little change in Al concentrations at $f_{O_2} < \text{QFM} + 0.5$ and decreasing Al at higher f_{O_2} , just as we
453 observe in our experimental spinels. MELTS captures this change in the substitution mechanism
454 for Fe³⁺ into spinel, replacing only Cr at f_{O_2} less than about QFM and replacing Al and Cr at
455 higher f_{O_2} better than the other two models.

456 SPINMELT and MELT-CHROMITE are at least partly empirical, and while their overall
457 accuracy in predicting spinel compositions is better than MELTS, they do not capture changes in
458 the cation exchange reactions seen the experiments. At f_{O_2} below QFM+2, SPINMELT

459 accurately predicts the ulvöspinel component (within ± 0.02 Fe²⁺ cations per formula unit) and
460 Fe³⁺ concentrations (within ± 0.09 cations per formula unit), but does not predict the high Fe³⁺
461 concentration of the most oxidizing experiment (Figure 7b). SPINMELT also accommodates all
462 of the Fe³⁺ increase with linearly decreasing Al, while Cr concentrations remain roughly
463 constant. This leads to variable accuracy in predicting Al concentrations (-0.13 to $+0.14$ cations
464 per formula unit) and consistent overestimation of Cr concentrations ($+0.03$ to $+0.21$ cations per
465 formula unit). This contrasts with the decrease in Cr observed in our experiments. SPINMELT's
466 inability to predict which trivalent cations will substitute for Fe³⁺ is consistent with the limited
467 range of Cr/Al in the calibration data used to formulate SPINMELT (Ariskin and Nikolaev 1996;
468 Poustovetov and Roeder 2001).

469 Of the models we examined, MELT-CHROMITE was most successful at accurately
470 predicting Fe³⁺ concentrations (within ± 0.05 cations per formula unit), and although it
471 consistently underestimated the ulvöspinel component, overall accuracy was good (-0.01 to -0.04
472 Fe²⁺ cations per formula unit). However, MELT-CHROMITE over-predicts Cr/Al ratios in
473 experiments more reducing than QFM+2 and under-predicts Cr/Al ratios of the most oxidizing
474 run. Importantly, MELT-CHROMITE predicts that spinel Al concentrations remain roughly
475 constant as f_{O_2} increases, with all additional Fe³⁺ being accommodated by decreasing Cr
476 concentrations. Instead, our experiments show that Fe³⁺ is accommodated by decreasing Cr and
477 Al above QFM.

478 The comparison of the model results to our experiments highlights the need for additional
479 experimental spinel compositions produced over a range of f_{O_2} to feed the next generation of
480 spinel models. Although SPINMELT and MELT-CHROMITE are reasonably accurate, their
481 inability to capture changes in the trivalent cation exchange reactions suggest that they will not

482 perform well outside their calibration ranges (for example, at high pressures), nor will they be
483 able to accurately predict changes to dynamic systems. Modeling near-fractional melting of
484 peridotite in the upper mantle will require Cr, Al, and Fe³⁺ exchange be modeled accurately.
485 Inaccuracies in how these cations exchange will be compounded over each melting step and will
486 tend to move the bulk composition of the system away from the behavior of the natural system,
487 even if any individual step produces relatively accurate spinel compositions.

488 Given the sophisticated nature of MELTS and the clear desire by the community to use it
489 to model partial melting of the mantle (e.g., Hirschmann et al. 1999; Asimow et al. 2001;
490 Coogan et al. 2004; Gaffney et al. 2005; Lambart et al. 2009; Byerly and Lassiter 2014), it is
491 worth further investigating the inaccurate predictions by MELTS of Cr and Fe³⁺ concentrations
492 in spinels at a given f_{O_2} . The extent of the problem can be demonstrated by comparing the
493 activities of magnetite ($a_{Fe_3O_4}^{spl}$) in experimental and model spinels (Figure 9). We have calculated
494 $a_{Fe_3O_4}^{spl}$ of the spinels from our experiments and those spinel compositions output by MELTS
495 using the MELTS Supplemental Calculator (Sack and Ghiorso 1991a, 1991b; [http://melts.ofm-](http://melts.ofm-research.org/CalcForms/index.html)
496 [research.org/CalcForms/index.html](http://melts.ofm-research.org/CalcForms/index.html)). At a given f_{O_2} , MELTS predicts spinels with $a_{Fe_3O_4}^{spl}$ 0.6 to
497 0.9 log units higher than in the spinels that are produced experimentally. Magnetite activity is the
498 variable with the greatest leverage over the calculation of f_{O_2} from olivine-orthopyroxene-spinel
499 equilibria, and it is difficult to reconcile this great a difference in $a_{Fe_3O_4}^{spl}$ in spinels nominally
500 recording the same f_{O_2} .

501 In two of our MELTS runs, the model predicted co-saturation of olivine, orthopyroxene,
502 and spinel at temperatures between 1225 °C and 1200 °C, allowing us to independently calculate
503 f_{O_2} from the output mineral compositions. We recalculated f_{O_2} of these model assemblages using

504 the oxybarometer of Mattioli and Wood (1988) (equation 4 of Davis et al. 2017) and using the
505 MELTS supplemental Calculator to calculate $a_{Fe_3O_4}^{spl}$. The combination of this oxybarometer and
506 method of calculating magnetite activity in spinel has been shown to accurately reproduce
507 experimental f_{O_2} at 0.1 MPa (Wood 1990; Herd 2008; Davis et al. 2017). In each case, f_{O_2}
508 calculated from the experimental mineral compositions accurately predicts the furnace f_{O_2} , but
509 the MELTS model run predicts f_{O_2} that is ~ 1.2 log units too high (Supplementary Table S4). This
510 suggests that MELTS can produce a peridotite solid assemblage that is out of redox equilibrium
511 with a coexisting liquid by greater than a log unit of f_{O_2} . AlphaMELTS provides an option that
512 allows the system to calculate f_{O_2} from the solid assemblage rather than from the melt
513 composition (ALTERNATIVE_FO2). We also ran alphaMELTS with ALTERNATIVE_FO2
514 turned on, and found that, although spinel Fe_2O_3 is slightly lower and Cr_2O_3 slightly higher than
515 with this option turned off, there is negligible effect on calculated f_{O_2} (Supplementary Table S4).

516 *Experimental melt fraction and the limited solidus depression caused by Fe^{3+}*

517 Given the expectation that Fe^{3+} should behave incompatibly during peridotite partial
518 melting (Canil et al. 1994), it is notable that experimental melt fraction remains constant in the
519 experimental series as the only bulk compositional change is in the ratio of Fe_2O_3/FeO (Figure
520 5a). It may be that the modest solidus depressing power of Fe^{3+} is partially offset by a
521 corresponding increase in Mg# of olivine and orthopyroxene, but our data also demonstrate that
522 Fe^{3+} becomes increasingly compatible in spinel as f_{O_2} increases (Figure 10) and Fe^{3+} constitutes a
523 greater proportion of the B-type cations. The increasing compatibility of Fe^{3+} as the magnetite
524 component in spinel increases is an important and interesting result of our study. At this time, we
525 do not have enough information to say definitively why Fe^{3+} becomes more compatible in spinel
526 as f_{O_2} increases, though we can speculate. It is likely that progressive changes in spinel chemistry

527 lessen the mismatch between the ionic radius of Fe^{3+} and the lattice site in which it sits, creating
528 more favorable site geometry for Fe^{3+} on the octahedral site, and possibly the tetrahedral site as
529 well. It is beyond the scope of this paper to determine the site specificity of Fe^{3+} accommodation
530 in spinel, but Fe^{3+} 's increased compatibility at constant melt fraction as f_{O_2} increases has
531 important consequences for melting in Earth.

532 Instead of promoting melting, increasing bulk $\text{Fe}^{3+}/\Sigma\text{Fe}$ ratios in peridotites drive
533 reactions analogous to the fayalite-ferrosilite-magnetite reaction (eq. 1). Fe^{3+} may become less
534 incompatible in bulk peridotite as it becomes more abundant by both increasing modal spinel and
535 increasing the spinel/melt partition coefficient of Fe^{3+} -- effectively cancelling any solidus-
536 depressing capability that Fe^{3+} might otherwise have. If this interpretation is correct, then there is
537 no reason to expect $\text{Fe}^{3+}/\Sigma\text{Fe}$ ratios of basalts to correlate with other incompatible elements once
538 the effects of low-pressure fractionation are corrected for, which may partly explain the absence
539 of correlation between Na_2O and Fe_2O_3 in fractionation-corrected MORB (Bézous and Humler
540 2005; Cottrell and Kelley 2011).

541 **Implications**

542 Our comparison between f_{O_2} calculated from olivine, orthopyroxene, and spinel mineral
543 analyses by electron microprobe and f_{O_2} calculated from $\text{Fe}^{3+}/\Sigma\text{Fe}$ ratios of basaltic glasses
544 measured by XANES demonstrates that these methods are both accurate and directly
545 comparable. Focus must now shift to whether f_{O_2} recorded by peridotites and basalts drawn from
546 the same tectonic settings can be corrected for the effects of petrological processes after
547 separation of melts from peridotite residues to reveal f_{O_2} conditions in melting source regions. To
548 a degree, this problem has already been solved for MORB. Decompression of a basaltic liquid as
549 it rises from a magma chamber to the surface causes a small (~ 0.25 log unit), predictable change

550 in f_{O_2} relative to QFM (Kress and Carmichael 1991), and the effects of olivine fractionation on
551 MORB $Fe^{3+}/\Sigma Fe$ ratios can also be corrected back to equilibrium with mantle olivine (Cottrell
552 and Kelley 2011).

553 Correcting peridotite f_{O_2} back to magma source conditions is more complex. Peridotites
554 from many different tectonic settings invariably record colder temperatures than magmatic
555 conditions (e.g., Bryndzia and Wood 1990; Woodland et al. 1992; Nasir 1996; Parkinson and
556 Arculus 1999). Simply recalculating f_{O_2} of a given spinel peridotite at higher temperatures leads
557 to a decrease in f_{O_2} relative to QFM. Temperature enters into the f_{O_2} calculation directly and in
558 the calculations of magnetite and fayalite activities; therefore, the effects of temperature are
559 compositionally dependent, but may be as much as -0.2 log units relative to QFM per 100 °C
560 (Davis et al. 2017). It is not sufficient to perform calculations at a hotter temperature without also
561 accounting for metamorphic reactions that have occurred upon cooling. Canil and O'Neill (1996)
562 suggested that as peridotites cool, spinel exsolves from pyroxenes, leading to dilution of the
563 magnetite component. This effect should tend to lower f_{O_2} of the peridotite, counter to the effect
564 of temperature on the calculation of f_{O_2} . Voigt and von der Handt (2011) developed a model for
565 calculating changing Cr# and modal proportion of spinel in peridotites upon cooling, but the
566 model does not take into account exchange of Fe^{3+} between spinel and pyroxenes. As we
567 demonstrated, MELTS is not able to accurately predict spinel compositions at a given f_{O_2} , so
568 there is currently no model available that can estimate the effects of metamorphic reactions in a
569 cooling spinel peridotite on recorded f_{O_2} . There is a clear need for additional experimental
570 constraints on spinel compositional variability in equilibrium with olivine and pyroxene across a
571 range of f_{O_2} .

572 More accurate spinel compositional models are not only needed to reconcile the MORB
573 and abyssal peridotite f_{O_2} data, but also to allow for reconstruction of mantle f_{O_2} conditions at
574 depths equal to and greater than the region of MORB melting. How f_{O_2} changes as a function of
575 depth in Earth's upper mantle affects phase stability (Stagno and Frost 2010; Rohrbach et al.
576 2011; Stagno et al. 2013) and rheological properties of the mantle (Keefner et al. 2011). MORB
577 glasses and abyssal peridotites anchor that redox profile. Because spinel composition is the
578 variable with the greatest leverage over the f_{O_2} recorded by the solids, accurate modeling of the
579 evolution of spinel compositions during melt extraction are required for any forward model of
580 mantle melting. Our MELTS modeling suggests that MELTS predicts residues that are too
581 oxidized to have equilibrated with the coexisting liquid phase. It is not obvious how this would
582 affect a multistep, fractional melting calculation in MELTS. On one hand, it may be that MELTS
583 will produce a series of fractional melts that are each more reduced than should be produced
584 from the equilibrium solid assemblage at any given step, this might lead MELTS to under-
585 predict f_{O_2} in the aggregate melt. On the other hand, at any given step, the liquid is extracting too
586 little Fe^{3+} from the residue, so the residue may evolve along a more oxidized trajectory than in
587 nature. Thinking outside of MELTS, we can reasonably ask the questions: Is incompatible Fe^{3+}
588 successively depleted in peridotite residues as melts are extracted, leading to decreasing f_{O_2}
589 relative to QFM as melting proceeds (e.g., Canil et al. 1994)? Or does Al- Fe^{3+} exchange between
590 spinel and melt, which favors increasing spinel Fe^{3+}/Al ratios as melting proceeds (Ballhaus et al.
591 1991), lead to an increase, or perhaps no change, in the f_{O_2} of the mantle as melts are extracted?
592 Our results suggest that the toolbox is not yet up to the job of answering these questions.

593 **Acknowledgements**

594 We thank Suzanne Birner and Paul Asimow for helpful discussions. We acknowledge support
595 from NSF OCE-1433212 and a Smithsonian National Museum of Natural History Peter Buck
596 Fellowship to FD. We are grateful for assistance from Tony Lanzirotti, Sue Wirick, Tim
597 Gooding and Tim Rose. This paper was improved by constructive reviews from N. Métrich and
598 an anonymous reviewer. We appreciated support of X26A from Department of Energy (DOE)
599 GeoSciences DE-FG02-92ER14244. The DOE Office of Science supported use of the NSLS
600 under Contract No. DE-AC02-98CH10886.

601 **References**

- 602 Ariskin, A.A., and Nikolaev, G.S. (1996) An empirical model for the calculation of spinel-melt equilibria
603 in mafic igneous systems at atmospheric pressure: 1. Chromian spinels. Contributions to
604 Mineralogy and Petrology, 123, 282–292.
- 605 Armstrong, J. (1988) Quantitative analysis of silicate and oxide minerals: comparison of Monte Carlo,
606 ZAF and phi-rho-z procedures. Microbeam analysis, 23, 239–246.
- 607 Asimow, P.D., and Ghiorso, M.S. (1998) Algorithmic modifications extending MELTS to calculate
608 subsolidus phase relations. American Mineralogist, 83, 1127–1132.
- 609 Asimow, P.D., Hirschmann, M., and Stolper, E. (2001) Calculation of peridotite partial melting from
610 thermodynamic models of minerals and melts, IV. Adiabatic decompression and the composition
611 and mean properties of mid-ocean ridge basalts. Journal of Petrology, 42, 963–998.
- 612 Ballhaus, C. (1995) Is the upper mantle metal-saturated? Earth and Planetary Science Letters, 132, 75–86.
- 613 Ballhaus, C., Berry, R., and Green, D. (1991) High pressure experimental calibration of the olivine-
614 orthopyroxene-spinel oxygen geobarometer: implications for the oxidation state of the upper
615 mantle. Contributions to Mineralogy and Petrology, 107, 27–40.

- 616 Barnes, S.J. (1986) The distribution of chromium among orthopyroxene, spinel and silicate liquid at
617 atmospheric pressure. *Geochimica et Cosmochimica Acta*, 50, 1889–1909.
- 618 Bastin, G., Van Loo, F., Vosters, P., and Vrolijk, J. (1983) A correction procedure for characteristic
619 fluorescence encountered in microprobe analysis near phase boundaries. *Scanning*, 5, 172–183.
- 620 Bézoz, A., and Humler, E. (2005) The Fe³⁺/ΣFe ratios of MORB glasses and their implications for
621 mantle melting. *Geochimica et Cosmochimica Acta*, 69, 711–725.
- 622 Brunelli, D., Seyler, M., Cipriani, A., Ottolini, L., and Bonatti, E. (2006) Discontinuous melt extraction
623 and weak refertilization of mantle peridotites at the Vema lithospheric section (Mid-Atlantic
624 Ridge). *Journal of Petrology*, 47, 745–771.
- 625 Bryndzia, L.T., and Wood, B.J. (1990) Oxygen thermobarometry of abyssal spinel peridotites: the redox
626 state and C–O–H volatile composition of the Earth’s sub-oceanic upper mantle. *American Journal
627 of Science*, 290, 1093–1116.
- 628 Byerly, B.L., and Lassiter, J.C. (2014) Isotopically ultradepleted domains in the convecting upper mantle:
629 Implications for MORB petrogenesis. *Geology*, 42, 203–206.
- 630 Canil, D., and O’Neill, H.S.C. (1996) Distribution of ferric iron in some upper-mantle assemblages.
631 *Journal of Petrology*, 37, 609–635.
- 632 Canil, D., Virgo, D., and Scarfe, C.M. (1990) Oxidation state of mantle xenoliths from British Columbia,
633 Canada. *Contributions to Mineralogy and Petrology*, 104, 453–462.
- 634 Canil, D., O’Neill, H.S.C., Pearson, D., Rudnick, R., McDonough, W., and Carswell, D. (1994) Ferric
635 iron in peridotites and mantle oxidation states. *Earth and Planetary Science Letters*, 123, 205–
636 220.

- 637 Coogan, L.A., Thompson, G., MacLeod, C.J., Dick, H., Edwards, S., Scheirer, A.H., and Barry, T.L.
638 (2004) A combined basalt and peridotite perspective on 14 million years of melt generation at the
639 Atlantis Bank segment of the Southwest Indian Ridge: evidence for temporal changes in mantle
640 dynamics? *Chemical Geology*, 207, 13–30.
- 641 Cottrell, E., and Kelley, K.A. (2011) The oxidation state of Fe in MORB glasses and the oxygen fugacity
642 of the upper mantle. *Earth and Planetary Science Letters*, 305, 270–282.
- 643 Cottrell, E., Kelley, K.A., Lanzirotti, A., and Fischer, R.A. (2009) High-precision determination of iron
644 oxidation state in silicate glasses using XANES. *Chemical Geology*, 268, 167–179.
- 645 Cottrell, E., Lanzirotti, A., Mysen, B.O., Birner, S.K., Kelley, K.A., Botcharnikov, Roman, Davis, Fred
646 A, and Newville, M (2018) A Mössbauer-based XANES calibration for hydrous basalt glasses
647 reveals radiation induced oxidation of Fe. *American Mineralogist*.
- 648 Danyushevsky, L.V., and Plechov, P. (2011) Petrolog3: Integrated software for modeling crystallization
649 processes. *Geochemistry, Geophysics, Geosystems*, 12.
- 650 Dasgupta, R., Mallik, A., Tsuno, K., Withers, A.C., Hirth, G., and Hirschmann, M.M. (2013) Carbon-
651 dioxide-rich silicate melt in the Earth's upper mantle. *Nature*, 493, 211–215.
- 652 Davis, F.A., Cottrell, E., Birner, S.K., Warren, J.M., and Lopez, O.G. (2017) Revisiting the electron
653 microprobe method of spinel-olivine-orthopyroxene oxybarometry applied to spinel peridotites.
654 *American Mineralogist*, 102, 421–435.
- 655 Frost, B.R. (1991) Introduction to oxygen fugacity and its petrologic importance. *Reviews in Mineralogy*
656 and *Geochemistry*, 25, 1–9.

- 657 Gaffney, A.M., Nelson, B.K., and Blichert-Toft, J. (2005) Melting in the Hawaiian plume at 1–2 Ma as
658 recorded at Maui Nui: the role of eclogite, peridotite, and source mixing. *Geochemistry,*
659 *Geophysics, Geosystems*, 6.
- 660 Ghiorso, M.S., and Sack, R.O. (1995) Chemical mass transfer in magmatic processes IV. A revised and
661 internally consistent thermodynamic model for the interpolation and extrapolation of liquid-solid
662 equilibria in magmatic systems at elevated temperatures and pressures. *Contributions to*
663 *Mineralogy and Petrology*, 119, 197–212.
- 664 Ghiorso, M.S., Hirschmann, M.M., Reiners, P.W., and Kress, V.C. (2002) The pMELTS: A revision of
665 MELTS for improved calculation of phase relations and major element partitioning related to
666 partial melting of the mantle to 3 GPa. *Geochemistry, Geophysics, Geosystems*, 3, 1–35.
- 667 Grove, T.L., Elkins-Tanton, L.T., Parman, S.W., Chatterjee, N., Müntener, O., and Gaetani, G.A. (2003)
668 Fractional crystallization and mantle-melting controls on calc-alkaline differentiation trends.
669 *Contributions to Mineralogy and Petrology*, 145, 515–533.
- 670 Herd, C.D. (2008) Basalts as probes of planetary interior redox state. *Reviews in Mineralogy and*
671 *Geochemistry*, 68, 527–553.
- 672 Hirschmann, M., Asimow, P.D., Ghiorso, M., and Stolper, E. (1999) Calculation of peridotite partial
673 melting from thermodynamic models of minerals and melts. III. Controls on isobaric melt
674 production and the effect of water on melt production. *Journal of Petrology*, 40, 831–851.
- 675 Hirschmann, M., Ghiorso, M., Davis, F., Gordon, S., Mukherjee, S., Grove, T., Krawczynski, M.,
676 Medard, E., and Till, C. (2008) Library of Experimental Phase Relations (LEPR): A database and
677 Web portal for experimental magmatic phase equilibria data. *Geochemistry, Geophysics,*
678 *Geosystems*, 9.

- 679 Ionov, D., and Wood, B. (1992) The oxidation state of subcontinental mantle: oxygen thermobarometry
680 of mantle xenoliths from central Asia. *Contributions to Mineralogy and Petrology*, 111, 179–193.
- 681 Johnson, K., and Dick, H.J. (1992) Open system melting and temporal and spatial variation of peridotite
682 and basalt at the Atlantis II fracture zone. *Journal of Geophysical Research: Solid Earth*, 97,
683 9219–9241.
- 684 Keefner, J., Mackwell, S., Kohlstedt, D., and Heidelbach, F. (2011) Dependence of dislocation creep of
685 dunite on oxygen fugacity: implications for viscosity variations in Earth’s mantle. *Journal of*
686 *Geophysical Research: Solid Earth*, 116.
- 687 Kress, V., and Carmichael, I. (1988) Stoichiometry of the iron oxidation reaction in silicate melts.
688 *American Mineralogist*, 73, 1267–1274.
- 689 Kress, V.C., and Carmichael, I.S. (1991) The compressibility of silicate liquids containing Fe₂O₃ and the
690 effect of composition, temperature, oxygen fugacity and pressure on their redox states.
691 *Contributions to Mineralogy and Petrology*, 108, 82–92.
- 692 Lambart, S., Laporte, D., and Schiano, P. (2009) An experimental study of focused magma transport and
693 basalt–peridotite interactions beneath mid-ocean ridges: implications for the generation of
694 primitive MORB compositions. *Contributions to Mineralogy and Petrology*, 157, 429–451.
- 695 Llovet, X., Valovirta, E., and Heikinheimo, E. (2000) Monte Carlo simulation of secondary fluorescence
696 in small particles and at phase boundaries. *Microchimica Acta*, 132, 205–212.
- 697 Luhr, J.F., and Aranda-Gómez, J.J. (1997) Mexican peridotite xenoliths and tectonic terranes: correlations
698 among vent location, texture, temperature, pressure, and oxygen fugacity. *Journal of Petrology*,
699 38, 1075–1112.

- 700 Mallmann, G., and O'Neill, H.S.C. (2009) The crystal/melt partitioning of V during mantle melting as a
701 function of oxygen fugacity compared with some other elements (Al, P, Ca, Sc, Ti, Cr, Fe, Ga, Y,
702 Zr and Nb). *Journal of Petrology*, 50, 1765–1794.
- 703 Mattioli, G.S., and Wood, B.J. (1988) Magnetite activities across the MgAl₂O₄-Fe₃O₄ spinel join, with
704 application to thermobarometric estimates of upper mantle oxygen fugacity. *Contributions to
705 Mineralogy and Petrology*, 98, 148–162.
- 706 Nasir, S. (1996) Oxygen thermobarometry of the Semail harzburgite massif, Oman and United Arab
707 Emirates. *European Journal of Mineralogy*, 153–164.
- 708 O'Neill, H.S.C., and Wall, V. (1987) The Olivine—Orthopyroxene—Spinel oxygen geobarometer, the
709 nickel precipitation curve, and the oxygen fugacity of the Earth's Upper Mantle. *Journal of
710 Petrology*, 28, 1169–1191.
- 711 Parkinson, I.J., and Arculus, R.J. (1999) The redox state of subduction zones: insights from arc-
712 peridotites. *Chemical Geology*, 160, 409–423.
- 713 Parkinson, I.J., and Pearce, J.A. (1998) Peridotites from the Izu–Bonin–Mariana forearc (ODP Leg 125):
714 evidence for mantle melting and melt–mantle interaction in a supra-subduction zone setting.
715 *Journal of Petrology*, 39, 1577–1618.
- 716 Poustovetov, A., and Roeder, P. (2001) Numerical modeling of major element distribution between
717 chromian spinel and basaltic melt, with application to chromian spinel in MORBs. *Contributions
718 to Mineralogy and Petrology*, 142, 58–71.
- 719 Rampone, E., Hofmann, A.W., and Raczek, I. (1998) Isotopic contrasts within the Internal Liguride
720 ophiolite (N. Italy): the lack of a genetic mantle–crust link. *Earth and Planetary Science Letters*,
721 163, 175–189.

- 722 Rohrbach, A., Ballhaus, C., Ulmer, P., Golla-Schindler, U., and Schönbohm, D. (2011) Experimental
723 evidence for a reduced metal-saturated upper mantle. *Journal of Petrology*, 52, 717–731.
- 724 Sack, R.O., and Ghiorso, M.S. (1991a) An internally consistent model for the thermodynamic properties
725 of Fe- Mg-titanomagnetite-aluminate spinels. *Contributions to Mineralogy and Petrology*, 106,
726 474–505.
- 727 ——— (1991b) Chromian spinels as petrogenetic indicators; thermodynamics and petrological
728 applications. *American Mineralogist*, 76, 827–847.
- 729 Smith, P.M., and Asimow, P.D. (2005) Adiatat_1ph: A new public front-end to the MELTS, pMELTS,
730 and pHMELTS models. *Geochemistry, Geophysics, Geosystems*, 6.
- 731 Stagno, V., and Frost, D.J. (2010) Carbon speciation in the asthenosphere: Experimental measurements of
732 the redox conditions at which carbonate-bearing melts coexist with graphite or diamond in
733 peridotite assemblages. *Earth and Planetary Science Letters*, 300, 72–84.
- 734 Stagno, V., Ojwang, D.O., McCammon, C.A., and Frost, D.J. (2013) The oxidation state of the mantle
735 and the extraction of carbon from Earth's interior. *Nature*, 493, 84–88.
- 736 Stormer, J.C. (1983) The effects of recalculation on estimates of temperature and oxygen fugacity from
737 analyses of multicomponent iron-titanium oxides. *American Mineralogist*, 68, 586–594.
- 738 Voigt, M., and von der Handt, A. (2011) Influence of subsolidus processes on the chromium number in
739 spinel in ultramafic rocks. *Contributions to Mineralogy and Petrology*, 162, 675–689.
- 740 Warren, J.M., and Shimizu, N. (2010) Cryptic variations in abyssal peridotite compositions: evidence for
741 shallow-level melt infiltration in the oceanic lithosphere. *Journal of Petrology*, 51, 395–423.

- 742 Wilke, M., Partzsch, G.M., Bernhardt, R., and Lattard, D. (2005) Determination of the iron oxidation state
743 in basaltic glasses using XANES at the K-edge. *Chemical Geology*, 220, 143–161.
- 744 Wood, B.J. (1990) An experimental test of the spinel peridotite oxygen barometer. *Journal of Geophysical*
745 *Research: Solid Earth*, 95, 15845–15851.
- 746 Wood, B.J., and Virgo, D. (1989) Upper mantle oxidation state: Ferric iron contents of Iherzolite spinels
747 by ^{57}Fe Mössbauer spectroscopy and resultant oxygen fugacities. *Geochimica et Cosmochimica*
748 *Acta*, 53, 1277–1291.
- 749 Woodland, A.B., Kornprobst, J., and Wood, B.J. (1992) Oxygen thermobarometry of orogenic Iherzolite
750 massifs. *Journal of Petrology*, 33, 203–230.
- 751 Xirouchakis, D., Hirschmann, M.M., and Simpson, J.A. (2001) The effect of titanium on the silica content
752 and on mineral-liquid partitioning of mantle-equilibrated melts. *Geochimica et Cosmochimica*
753 *Acta*, 65, 2201–2217.
- 754 Zhang, H.L., Cottrell, E., Solheid, P.A., Kelley, K.A., and Hirschmann, M.M. (2018) Determination of Fe
755 $^{3+}/\Sigma\text{Fe}$ of XANES basaltic glass standards by Mössbauer spectroscopy and its application to the
756 oxidation state of iron in MORB. *Chemical Geology*.

757

758 **Figure Captions**

759 **Figure 1.** Back-scattered electron image of sample LOOS2_1.5A showing typical sizes and
760 textures of crystals grown in this study. Analysis of spinels by electron microprobe was
761 particularly challenging given the small size of these crystals.

762 **Figure 2.** Molar cation compositions of experimental spinels normalized to three total formula
763 cations. The x-axis shows $\log f_{\text{O}_2}$ (here and in subsequent figures f_{O_2} is in bars) relative to QFM
764 as measured by the EMF of the oxygen sensor during the experiment. Error bars show error at
765 1σ . Where error bars are absent, uncertainty is less than the size of the data symbol. Tie lines are
766 meant only to guide the reader where data series cross each other. **a.** A-type cations Mg, Ti, and
767 Fe^{2+} . **b.** B-type cations Al, Cr, Fe^{3+} , and Fe^{2+} associated with ulvöspinel component.

768 **Figure 3.** Major and minor element compositions of experimental glasses. White symbols
769 indicate the composition of experiment LOOS_0B, which used the LOOS starting material. Gray
770 symbols indicate glasses from experiments using the LOOS2 starting material. Error bars show
771 error at 1σ . Where error bars are absent, uncertainty is less than the size of the data symbol.

772 **Figure 4.** Mg# ($\text{Mg}/[\text{Mg}+\text{Fe}]$) of experimental olivines. Data symbols are as in Fig. 3. **a.** Olivine
773 Mg# calculated directly from EPMA analysis. **b.** Olivine Mg# corrected for the effects of Fe-
774 loss, demonstrating the effect that changes in f_{O_2} would have on Mg# of olivine in an inert
775 environment.

776 **Figure 5.** Modal proportions of phases (wt.%) determined from mass balance. Symbol colors are
777 as in Fig. 3. Error bars show standard error of the multiple linear regression, propagated through
778 renormalization after accounting for Fe-loss to the Pt loop. Bold black lines show linear
779 regression of the modal proportions of each phase against $\log f_{\text{O}_2}$ (ΔQFM) calculated only from
780 experiments using the LOOS2 starting material. **a.** Modal proportion of glass. **b.** Modal
781 proportion of spinel. Experiment LOOS_0B not shown because it plots out of frame at a modal
782 proportion of 10.4 ± 0.5 wt.%. **c.** Modal proportions of olivine and orthopyroxene.

783 **Figure 6.** Comparisons of different methods of calculating f_{O_2} in the experiments. Error bars
784 show 1σ errors. For spinel oxybarometry, 1σ errors were estimated from the standard error y-
785 intercept determined by regressing $Fe^{3+}/\Sigma Fe$ ratios calculated from individual microprobe
786 measurements against Na_2O , similar to the method used to determine spinel compositions. For
787 XANES, 1σ errors were calculated from the standard error given by (Kress and Carmichael
788 1988). Bold black line shows a 1:1 relationship between f_{O_2} calculated by each method being
789 compared. Bold gray line shows the linear regression between methods of calculating f_{O_2} . See
790 text for correlation coefficients, slopes, and intercepts of the regressions. **a.** $\text{Log}f_{O_2}$ calculated
791 from spinel oxybarometry plotted against $\text{log}f_{O_2}$ measured in the experimental gas mix. **b.** $\text{Log}f_{O_2}$
792 calculated from XANES measurement of $Fe^{3+}/\Sigma Fe$ in the glass plotted against $\text{log}f_{O_2}$ measured in
793 the experimental gas mix. **c.** Comparison of $\text{log}f_{O_2}$ calculated from Fe-XANES of the glass
794 against $\text{log}f_{O_2}$ calculated from spinel oxybarometry.

795 **Figure 7.** Comparison between experimental spinels from this study with model spinel
796 compositions calculated from three different models. Compositions are presented as modal
797 cations proportions per 3 total cations. Only B-type cations are shown. Gray symbols are
798 experimental compositions from this study with error bars as in Fig. 2. White symbols are model
799 output spinel compositions. Gray and black tie lines are meant only to aid the reader in
800 connecting data and model output series that cross or overlap one another. **a.** Model results from
801 MELTS (Ghiorso and Sack 1995), calculated using the alphaMELTS application (Asimow and
802 Ghiorso 1998; Ghiorso et al. 2002; Smith and Asimow 2005). Additional details given in the
803 text. **b.** Model results from SPINMELT (Ariskin and Nikolaev 1996) calculated using Petrolog 3
804 (Danyushevsky and Plechov 2011). Additional details given in text. **c.** Model results from
805 MELT-CHROMITE (Poustovetov and Roeder 2001).

806 **Figure 8.** Histograms of f_{O_2} measurements from MORB (Cottrell and Kelley 2011; Zhang et al.
807 2018) and abyssal peridotites (Bryndzia and Wood 1990). All literature data has been reported
808 relative to QFM following the formulation of Frost (1991). Consequently, averages are slightly
809 different than reported in some of the original sources.

810 **Figure 9.** Log activities of magnetite in the experimental (gray) and MELTS model (white)
811 spinels. Activities were calculated using the MELTS Supplemental Calculator (Sack and Ghiorso
812 1991a, 1991b; <http://melts.ofm-research.org/CalcForms/index.html>).

813 **Figure 10.** Effects of changing $\log f_{O_2}$ on spinel/melt partitioning of Fe^{3+} . Symbols are as in Fig.
814 3, and error bars are at 1σ . The best-fit line has slope = 0.43 ± 0.14 , y-intercept = 5.01 ± 0.17 , and
815 $R^2 = 0.62$ with p-value = 0.02.

816

Table 1. Compositions of experimental starting materials and model phase components as wt.% oxides
 modified melt and spinel components

	starting materials		phases from 85-41c#4 (Grove et al., 2003)				modified melt and spinel components	
	LOOS	LOOS2	glass	ol	opx	spl	melt	spl
SiO ₂	48.72	52.67	56.8	39.4	56.4	0.18	55.78	0.18
TiO ₂	2.25	2.20	0.93	0.02	0.09	0.43	3.00	1.39
Al ₂ O ₃	12.70	11.77	15.6	0.05	1.18	18.1	15.36	18.11
Cr ₂ O ₃	4.93	1.59	0.06	0.03	0.61	48.2	0.06	48.22
FeO*	8.20	7.38	6.71	11.5	6.26	17.8	6.61	17.81
MnO	0.09	0.09	0.07	0.17	0.13	0.1	0.07	0.10
MgO	14.26	15.10	6.89	47.8	32.8	14.1	6.78	14.10
CaO	6.06	6.28	8.48	0.28	1.68	0.1	8.35	0.10
Na ₂ O	2.30	2.36	3.33				3.28	
K ₂ O	0.50	0.51	0.73				0.72	
P ₂ O ₅			0.15					
NiO				0.18				
V ₂ O ₃		0.05						
total	100.00	100.00	99.75	99.43	99.15	99.01	100.00	100.00

817

818

Table 2. List of experimental details for 1-atm experiments at 1225 °C

experiment name	starting mix	furnace $\log f_{O_2}^a$	$\log f_{O_2}$ (ΔQFM^b)	duration (h)	phase proportions (wt.%)				Fe loss (% of ΣFe)	$\log f_{O_2}$ spl-oxybarometry	error	$\log f_{O_2}$ XANES ^c
					glass	ol	opx	spl				
LOOS2_-2A	LOOS2	-9.89	-1.87	70	76.1 (19)	12.5 (8)	8.7 (11)	2.8 (1)	18.7 (22)	-9.60	+0.47, -0.51	-9.72
LOOS2_-1B	LOOS2	-9.06	-1.04	73	75.4 (33)	11.0 (13)	10.7 (19)	2.9 (3)	6.5 (44)	-9.17	± 0.64	-9.26
LOOS2_-0.5A	LOOS2	-8.51	-0.49	72	74.6 (19)	7.7 (7)	14.7 (11)	2.9 (2)	10.6 (24)	-8.54	± 0.34	-8.78
LOOS_0B	LOOS	-8.13	-0.11	40	72.6 (30)	5.9 (12)	11.2 (18)	10.4 (5)	8.4 (40)	-8.81	+0.35, -0.38	-8.59
LOOS2_0.5A	LOOS2	-7.32	0.70	71	74.2 (19)	6.2 (7)	16.6 (11)	3.0 (2)	6.5 (26)	-7.62	± 0.32	-7.81
LOOS2_1B	LOOS2	-7.35	0.67	65	75.1 (20)	8.6 (8)	13.3 (12)	3.0 (2)	9.6 (26)	-7.39	+0.25, -0.26	-8.14
LOOS2_1.5A	LOOS2	-6.62	1.40	72	75.4 (18)	6.2 (7)	15.3 (10)	3.1 (2)	8.9 (23)	-7.11	± 0.20	-7.00
LOOS2_2A	LOOS2	-5.79 ^d	2.23	71	75.7 (19)	6.3 (7)	14.8 (11)	3.2 (2)	6.5 (25)	-6.20	+0.42, -0.40	-5.19

^a f_{O_2} in all instances is calculated in log bars

^bFormulation of Frost (1991)

^cStandard error of $\log f_{O_2}$ by XANES is ± 0.64 log units following the standard error given in Kress and Carmichael (1988)

^dSome fluctuation in the furnace EMF were recorded in the final 2 hours of this experiment, see text for details

Table 3. Spinel compositions given as wt.% oxides

experiment n	LOOS2_-2A 4	LOOS2_-1B 12	LOOS2_-0.5A 13	LOOS_0B 7	LOOS2_0.5A 5	LOOS2_1B 13	LOOS2_1.5A 5	LOOS2_2A 4
TiO ₂	1.95 (5)	2.24 (12)	2.13 (9)	2.15 (7)	2.03 (7)	2.07 (5)	2.00 (14)	1.56 (8)
Al ₂ O ₃	18.1 (5)	18.7 (10)	18.5 (10)	18.9 (10)	17.3 (4)	16.8 (5)	15.7 (9)	13.0 (9)
Cr ₂ O ₃	49.4 (3)	47.2 (12)	46.8 (14)	44.5 (9)	45.32 (18)	46.8 (4)	44.5 (15)	42.0 (13)
FeO*	12.7 (4)	15.08 (24)	15.5 (5)	16.5 (4)	17.1 (4)	16.99 (24)	19.9 (4)	23.4 (10)
MnO	0.162 (13)	0.172 (26)	0.168 (21)	0.160 (15)	0.17 (3)	0.177 (25)	0.193 (28)	0.186 (19)
MgO	15.97 (28)	14.95 (22)	15.37 (29)	15.5 (3)	15.3 (3)	14.7 (3)	15.16 (20)	15.6 (3)
Total	98.3	98.3	98.5	97.7	97.2	97.5	97.5	95.7
uncorrected Fe ³⁺ /ΣFe	0.090	0.105	0.175	0.245	0.284	0.223	0.383	0.558
corrected Fe ³⁺ /ΣFe	0.115 (17)	0.169 (20)	0.239 (14)	0.232 (26)	0.309 (21)	0.287 (16)	0.402 (11)	0.575 (10)
a _{mag}	0.000756	0.00239	0.00469	0.00545	0.00920	0.00778	0.0186	0.0402

FeO* is total Fe reported as FeO

Table 4. Glass compositions given as wt.% oxides

EPMA

measurements	LOOS2_-2A	LOOS2_-1B	LOOS2_-0.5A	LOOS_0B	LOOS2_0.5A	LOOS2_1B	LOOS2_1.5A	LOOS2_2A
n	20	15	15	10	15	15	15	14
SiO ₂	58.0 (13)	57.61 (28)	56.2 (6)	56.9 (4)	55.7 (8)	56.2 (7)	55.8 (8)	55.8 (5)
TiO ₂	2.82 (13)	2.76 (7)	2.68 (7)	2.65 (7)	2.69 (5)	2.67 (9)	2.62 (6)	2.63 (8)
Al ₂ O ₃	15.1 (3)	14.99 (28)	14.87 (2)	14.87 (16)	15.0 (3)	14.87 (16)	14.7 (3)	14.7 (4)
Cr ₂ O ₃	0.14 (5)	0.11 (3)	0.10 (4)	0.163 (27)	0.11 (4)	0.078 (26)	0.10 (4)	0.08 (4)
FeO*	5.2 (5)	6.35 (17)	6.02 (26)	6.54 (14)	6.44 (24)	5.95 (12)	6.2 (3)	6.4 (15)
MnO	0.09 (5)	0.07 (4)	0.08 (4)	0.09 (4)	0.10 (5)	0.08 (6)	0.08 (5)	0.08 (3)
MgO	7.8 (5)	7.99 (19)	8.22 (19)	8.35 (10)	8.27 (17)	8.13 (7)	8.52 (14)	8.49 (16)
CaO	8.2 (4)	8.37 (6)	8.21 (11)	8.28 (14)	8.29 (10)	8.23 (8)	8.08 (11)	8.09 (14)
Na ₂ O	3.07 (19)	2.92 (12)	3.11 (8)	3.02 (7)	3.08 (10)	3.02 (14)	3.16 (15)	3.06 (13)
K ₂ O	0.59 (6)	0.57 (4)	0.58 (4)	0.57 (4)	0.57 (5)	0.57 (3)	0.59 (4)	0.57 (4)
Total	101.01	101.74	100.07	101.433	100.25	99.798	99.85	99.9
XANES								
measurements								
n	3	3	2	2	3	4	3	2
average drift-corrected centroid (eV)	7112.092 (8)	7112.136 (8)	7112.197 (8)	7112.218 (17)	7112.335 (20)	7112.285 (16)	7112.478 (8)	7112.839 (20)
Fe ³⁺ /ΣFe ^a	0.076 (3)	0.091 (3)	0.111 (3)	0.119 (6)	0.162 (8)	0.143 (6)	0.219 (3)	0.386 (10)

^aFe³⁺/ΣFe = a₁ + a₂x + a₃x², where x is the drift-corrected centroid energy minus 7112.22 eV. a₁ = 0.120, a₂ = 0.354, and a₃ = 0.125 (Zhang et al. 2018)

821

822

Table 5. Olivine compositions given as wt.% oxides

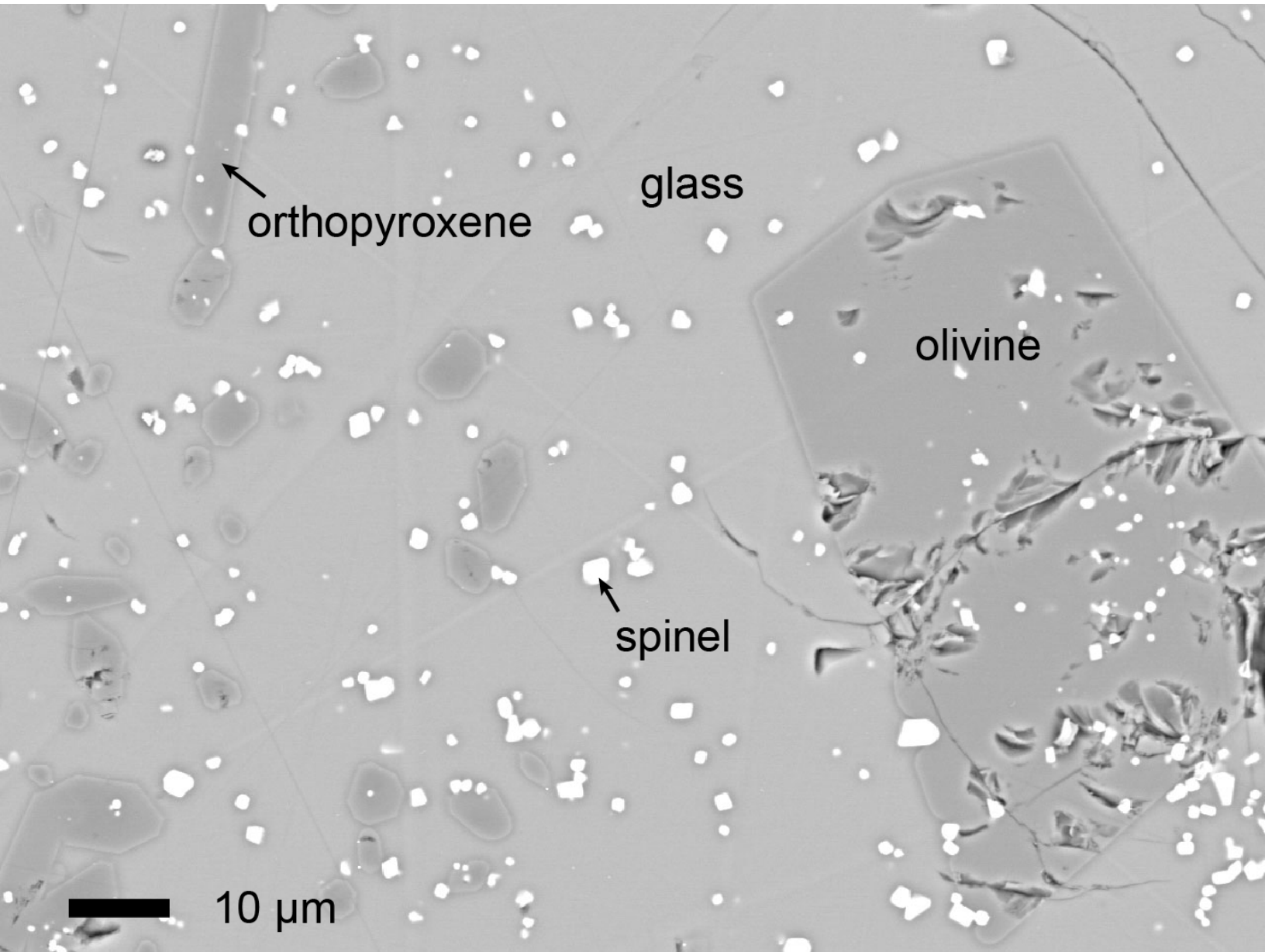
experiment n	LOOS2_-2A 15	LOOS2_-1B 15	LOOS2_-0.5A 14	LOOS_0B 13	LOOS2_0.5A 15	LOOS2_1B 15	LOOS2_1.5A 15	LOOS2_2A 15
SiO ₂	41.0 (3)	41.12 (5)	40.8 (4)	40.71 (20)	40.64 (29)	40.58 (14)	40.6 (4)	40.6 (3)
TiO ₂	0.043 (12)	0.034 (11)	0.036 (11)	0.037 (13)	0.032 (16)	0.038 (12)	0.035 (19)	0.043 (18)
Al ₂ O ₃	0.035 (14)	0.040 (11)	0.028 (9)	0.048 (22)	0.036 (9)	0.038 (14)	0.045 (23)	0.041 (13)
Cr ₂ O ₃	0.17 (3)	0.130 (25)	0.123 (11)	0.25 (5)	0.114 (24)	0.128 (17)	0.12 (6)	0.096 (14)
FeO*	9.8 (3)	10.5 (7)	10.6 (3)	10.08 (14)	10.15 (26)	9.69 (19)	9.75 (18)	8.8 (5)
MnO	0.113 (19)	0.114 (15)	0.112 (22)	0.107 (29)	0.118 (16)	0.106 (15)	0.111 (15)	0.107 (25)
MgO	49.3 (3)	48.3 (8)	48.6 (5)	49.5 (3)	48.8 (5)	48.8 (3)	49.36 (25)	50.0 (6)
CaO	0.199 (13)	0.196 (19)	0.210 (10)	0.189 (17)	0.194 (13)	0.195 (15)	0.181 (19)	0.19 (3)
Total	100.66	100.434	100.509	100.921	100.084	99.575	100.202	99.877
Mg#	0.900 (3)	0.891 (8)	0.891 (4)	0.897 (2)	0.896 (3)	0.900 (2)	0.900 (2)	0.910 (6)

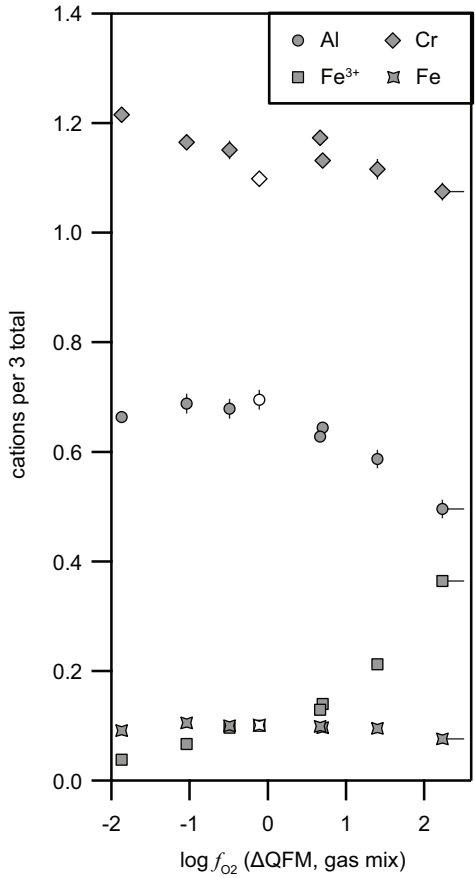
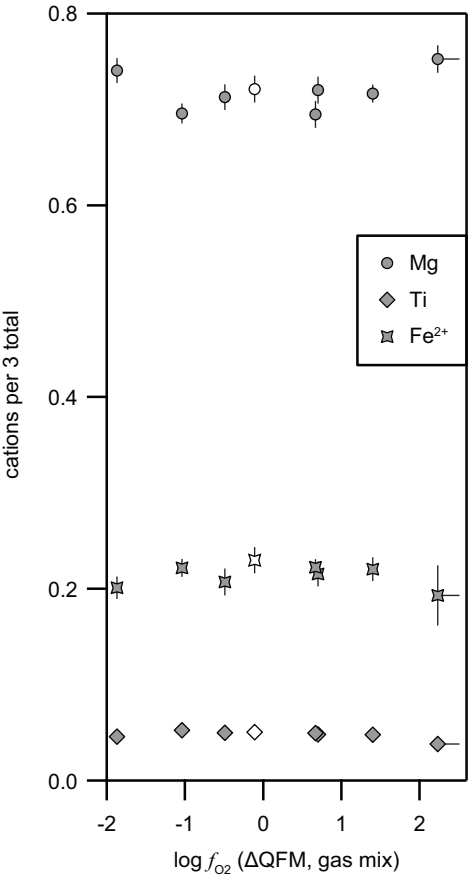
823

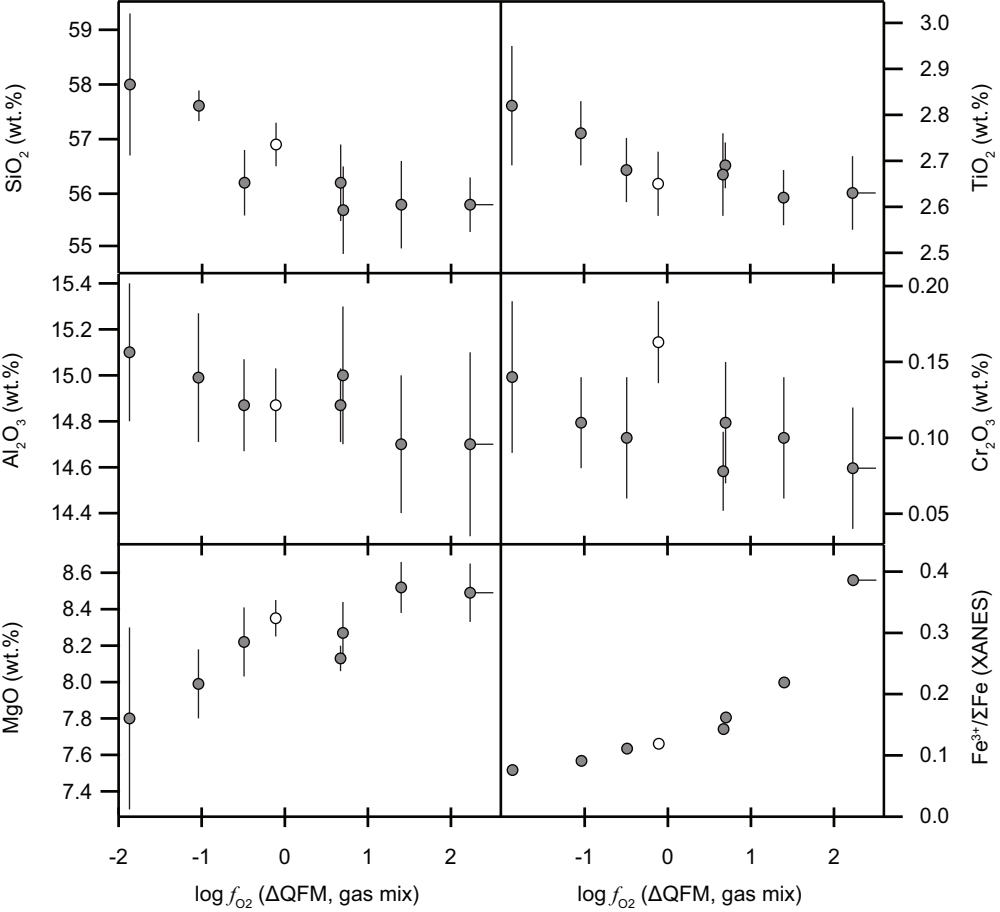
824

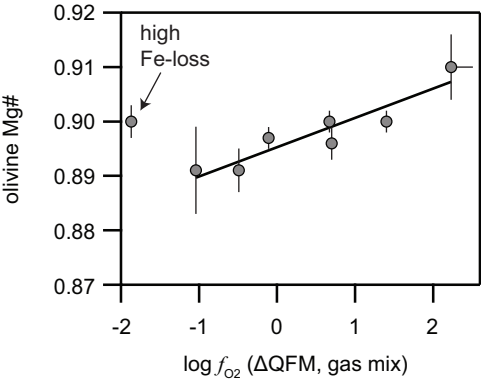
Table 6. Orthopyroxene compositions given as wt.% oxides

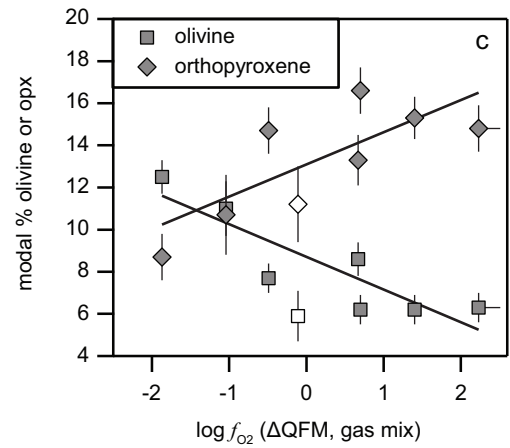
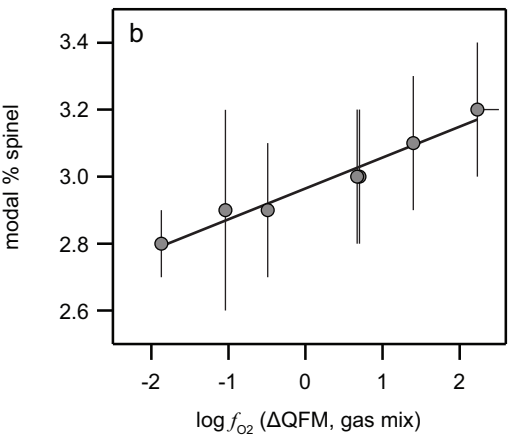
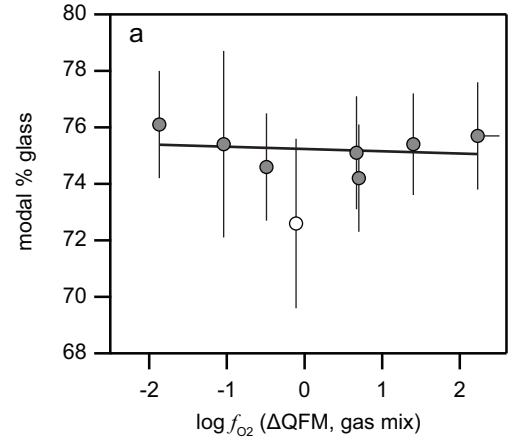
experiment n	LOOS2_-2A 13	LOOS2_-1B 12	LOOS2_-0.5A 15	LOOS_0B 10	LOOS2_0.5A 15	LOOS2_1B 15	LOOS2_1.5A 15	LOOS2_2A 14
SiO ₂	56.0 (8)	56.0 (5)	56.5 (3)	55.9 (4)	56.2 (6)	54.9 (6)	55.5 (6)	56.2 (5)
TiO ₂	0.45 (4)	0.47 (4)	0.45 (6)	0.479 (20)	0.41 (5)	0.43 (3)	0.43 (4)	0.424 (27)
Al ₂ O ₃	1.8 (5)	2.5 (5)	2.14 (27)	2.36 (11)	1.5 (4)	1.55 (17)	2.1 (4)	2.2 (4)
Cr ₂ O ₃	0.80 (15)	0.78 (12)	0.76 (15)	0.95 (9)	0.76 (18)	0.80 (13)	0.74 (15)	0.72 (14)
FeO*	5.96 (13)	5.6 (6)	5.7 (5)	4.5 (5)	5.9 (7)	6.26 (9)	5.3 (5)	4.8 (5)
MnO	0.104 (19)	0.095 (19)	0.103 (19)	0.101 (15)	0.094 (24)	0.099 (24)	0.104 (13)	0.099 (21)
MgO	33.9 (3)	33.6 (6)	33.9 (7)	35.5 (5)	33.7 (6)	33.2 (5)	34.4 (5)	34.8 (5)
CaO	1.34 (5)	1.37 (11)	1.38 (15)	1.51 (7)	1.39 (5)	1.30 (5)	1.21 (5)	1.27 (6)
Na ₂ O	0.021 (25)	0.05 (9)		0.007 (9)	0.023 (15)	0.029 (12)	0.023 (18)	0.016 (2)
Total	100.4	100.5	100.9	101.3	100.00	98.6	99.8	100.5
$X_{Fe}^{M1} \cdot X_{Fe}^{M2}$	0.0073 (3)	0.0065 (15)	0.0067 (12)	0.0040 (9)	0.0073 (19)	0.0084 (3)	0.0058 (11)	0.0047 (11)











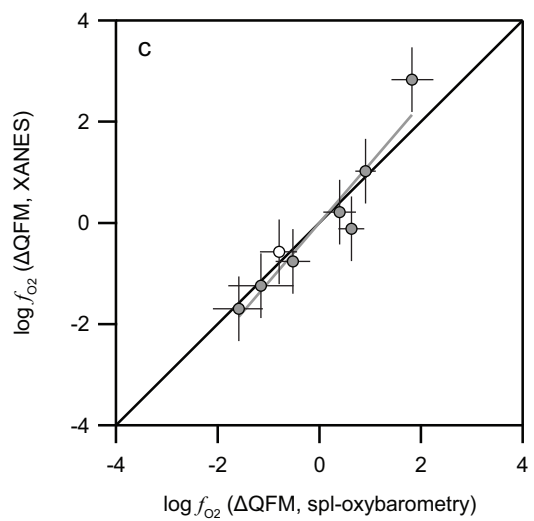
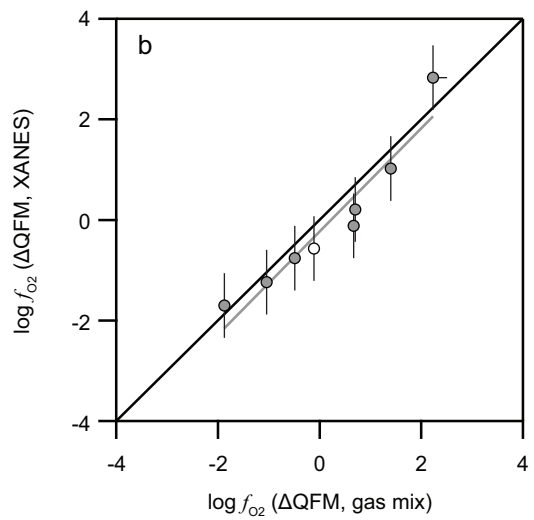
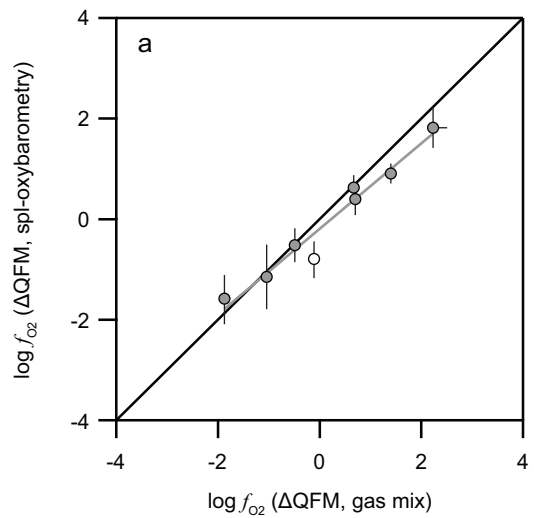
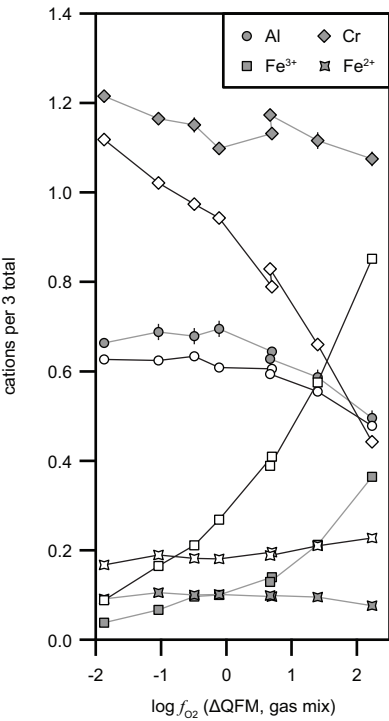
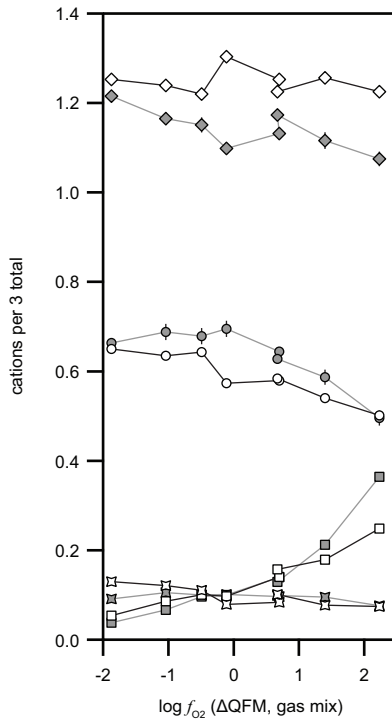


Figure 6

MELTS



SPINMELT



MELT-CHROMITE

